On the Magnetoelectric Properties and Elementary Excitations in Fe^{3+} substituted $TbMnO_3$

André Maia
Mestrado em Física
Departamento de Física e Astronomia
2019

Orientador
Joaquim Agostinho Moreira, Professor Auxiliar, Faculdade de Ciências

Acknowledgments

All the samples used in this work were produced by the group of M. Mihalik at IEP-SAS. Some polar measurements with applied magnetic field were performed at FCUL, with the help and collaboration of M. M. Cruz and M. Godinho. All the measurements carried out at IFIMUP benefited from the tireless guidance of R. Vilarinho, to whom I am thankful. My stay at FZU in Prague, Czech Republic was possible due to the Erasmus+ internship programme and both the scientific supervision and remarkable support of S. Kamba. Regarding the experimental work carried out there, I would like to point out the great aid of P. Proschek and Jan Prokleška in the polar and dielectric measurements, as well as that of C. Kadlec and F. Kadlec in the THz time-domain spectroscopy measurements. Last but not least, I am thankful to J. Agostinho Moreira for his outstandingly devoted supervision.

I am genuinely grateful to my family and Rita, without whom none of this would be possible.

Resumo

Os multiferróicos, onde as ordens magnética e ferroelétrica coexistem e estão acopladas, têm atraído grande interesse. A coexistência de fases magnéticas e ferroelétricas nestes materiais origina efeitos importantes associados ao acoplamento cruzado entre parâmetros de ordem e campos externos. Estudos anteriores realizados em cerâmicos do multiferróico $TbMnO_3$ mostram que a substituição de Mn^{3+} por pequenas quantidades de Fe^{3+} muda profundamente as estruturas magnética e polar, alterando o acoplamento magnetoelétrico. No entanto, como tais estudos foram realizados em cerâmicos, não foi possível estudar a anisotropia da polarização elétrica e das propriedades magnéticas.

Nesta dissertação, cristais orientados de $TbMn_{1-x}Fe_xO_3$ com $x = 0,02$ e $0,04$ são utilizados para estudar as propriedades magnéticas, dielétricas, polares e magnetoelétricas versus temperatura e campo magnético aplicado. Resultados de difração de neutrões publicados em $TbMn_{0.98}Fe_{0.02}O_3$ são também discutidos em conexão com as medidas magnéticas e polares. Para compreender melhor os mecanismos microscópicos na região multiferróica do sistema $TbMn_{1-x}Fe_xO_3$, foram também realizados estudos de espectroscopia THz e Raman em função da temperatura. Nos compostos substituídos, é mostrado que ocorre uma diminuição da polarização com o aumento do campo magnético aplicado e que tal é devido a um aumento do spin-canting, que perturba a ordem cicloidal dos spins. É observado que as propriedades magnetoelétricas de $TbMn_{0.96}Fe_{0.04}O_3$ são surpreendentemente diferentes das de $TbMnO_3$, ocorrendo uma supressão da ferroeletricidade quando um campo magnético é aplicado ao longo de dois dos eixos cristalográficos. Em $TbMn_{0.96}Fe_{0.04}O_3$, dois eletromagnões são identificados, estando fortemente acoplados nas fases magneticamente ordenadas. Curiosamente, tal como em $TbMnO_3$, essas excitações são discerníveis bem acima de T_N. Isso, juntamente com um largo pico na magnetização perto de $120\,\mathrm{K}$ observado em todos os compostos e um salto na absorção detetado a $100\,\mathrm{K}$ em $TbMn_{0.96}Fe_{0.04}O_3$, apontam para um desenvolvimento de ordem magnética de curto alcance acima de T_N. Verificou-se que, em $TbMnO_3$, as oscilações Raman dos iões Tb^{3+} não são sensíveis às interações magnéticas, o que parece indicar que esses iões não interagem significativamente com a sub-rede Mn^{3+}. No entanto, apenas adicionando até 4% de Fe^{3+}, o modo Raman associado às oscilações de Tb^{3+} ao longo do eixo x torna-se sensível ao magnetismo do composto, indicando que os spins de Tb^{3+} começam a interagir com a sub-rede Mn^{3+}/Fe^{3+}. Notavelmente, o modo Raman associado às oscilações de Tb^{3+} ao longo do eixo z praticamente não deteta as interações magnéticas em nenhum dos compostos. Os resultados da magnetização, difração de neutrões e medidas polares, juntamente com a diferença no comportamento dos modos Raman nos compostos substituídos em relação ao $TbMnO_3$, apontam para um caráter ferromagnético emergente das estruturas magnéticas dos compostos substituídos.

Palavras-chave: Magnetoelétricos, Multiferróicos, Ferroeletricidade, Magnetismo, Electromagnões, Manganites ortorrômbicas de terras raras

Abstract

Multiferroics, where both magnetic and ferroelectric orders coexist and are coupled to one another, have attracted great interest. The coexistence of magnetic and ferroelectric phases in multiferroic materials gives rise to important effects associated with the cross correlation between order parameters and external fields. Previous studies performed in ceramics of the multiferroic $TbMnO_3$ show that the substitution of Mn^{3+} by small amounts of the identically sized Fe^{3+} ion profoundly changes both the magnetic and polar structures, altering the magnetoelectric coupling. As these studies were performed in ceramics, any anisotropic features exhibited by the electric polarization and magnetic properties could not be ascertained.

In this dissertation, oriented single crystals of $TbMn_{1-x}Fe_xO_3$ with $x = 0.02$ and 0.04 are used to study the magnetic, dielectric, polar and magnetoelectric properties versus temperature and applied magnetic field. Previously reported neutron diffraction results in $TbMn_{0.98}Fe_{0.02}O_3$ are also discussed in connection with the magnetic and polar measurements. To further understand the microscopic mechanisms in the multiferroic region of the $TbMn_{1-x}Fe_xO_3$ system, THz time-domain spectroscopy and Raman scattering experiments as a function of temperature were performed.

For the substituted compounds, an overall decrease in polarization with increasing applied magnetic field is shown to be due to an enhancement of a spin-canting that disrupts the cycloidal spin order. It is seen that the magnetoelectric properties of $TbMn_{0.96}Fe_{0.04}O_3$ are strikingly different from the ones of $TbMnO_3$, with a suppression of ferroelectricity occurring when a magnetic field is applied along two of the crystallographic axes. In $TbMn_{0.96}Fe_{0.04}O_3$, two electromagnons are identified and appear to be strongly coupled in the magnetically ordered phases. Interestingly, as in $TbMnO_3$, such excitations are already discernible at 250 K, a much higher temperature than T_N. This, together with a broad peak in magnetization around 120 K observed in all compounds and a jump in absorption detected at 100 K in $TbMn_{0.96}Fe_{0.04}O_3$, point towards a development of short-range spin order well above T_N. It was found that, in $TbMnO_3$, the Tb^{3+} oscillations are not sensitive to the magnetic interactions, which appears to indicate that those ions do not significantly interact with the Mn^{3+} sublattice. However, by adding only up to 4% of Fe^{3+}, the Raman mode associated with Tb^{3+} oscillations along the x axis becomes sensitive to the compound's magnetism, indicating that the Tb^{3+} spins begin to interact with the Mn^{3+}/Fe^{3+} sublattice. Remarkably, the Raman mode associated with Tb^{3+} oscillations along the z axis practically does not sense the magnetic interactions in any of the compounds. The results from magnetization, neutron diffraction and polar measurements, together with the difference in the behavior of the Raman modes in the substituted compounds relatively to $TbMnO_3$, all point towards an emerging FM character of the magnetic structures of the substituted compounds.

Keywords: Magnetoelectrics, Multiferroics, Ferroelectricity, Magnetism, Electromagnons, Rare-Earth Orthorhombic Manganites

Contents

List of Figures

List of Tables

Nomenclature

AFM	Antiferromagnetic
DM	Dzyaloshinsky-Moriya
FC	Field Cooling
FM	Ferromagnetic
HE-EMG	Higher Energy Electromagnon
JT	Jahn-Teller
LE-EMG	Lower Energy Electromagnon
ZFC	Zero Field Cooling

Chapter 1

Introduction

Magnetoelectric multiferroics, where spontaneous long-range magnetic and dipolar order coexist, represent a very attractive class of compounds combining rich and fascinating fundamental physics with a potential for multifunctional applications. The first definition of multiferroicity dates back to 1994, when Schmid referred to multiferroics as a class of materials which simultaneously exhibit more than one primary ferroic order parameter in a single phase [1]. However, the finding of a strong coupling between magnetic and electric degrees of freedom in insulators can be traced back to Pierre Curie and, in 1959, Landau and Lifshitz made a short remark about the subject in a volume of their Course of Theoretical Physics [2, 3]. While materials that are simultaneously ferroelectric and ferroelastic or ferromagnetic and ferroelastic are formally multiferroics, nowadays the term is frequently employed to describe magnetoelectric multiferroics, simultaneously ferromagnetic and ferroelectric, even though magnetoelectrics are not necessarily multiferroic. However, from this point forward, magnetoelectric multiferroics will be simply referred to as multiferroics. As a successive hot topic in correlated electronic materials after high temperature superconductors and colossal magnetoresistive manganites, multiferroics have attracted enormous attention in the past decade [4, 5, 6, 7]. Several promising technological applications include the ability to electrically address magnetic memory (without currents), the creation of new types of 4-state logic (i.e., with both up and down polarization and up and down magnetization) and magnetoelectric sensors [2, 7]. Thus, multiferroic research in the past decade has been triggered both by eventual applications and scientific curiosity, as the discovery of multiferroicity breaks the apparent mutual exclusion between magnetic moments and electric dipoles [8]. In 2009, Khomskii proposed a classification of multiferroics into two categories [2]. The first, type-I multiferroics, contains those materials in which the stability regions of the ferroelectric and magnetic phases do not coincide, implying that such orderings have different origins. In these materials, ferroelectricity typically appears at higher temperatures than magnetism and the spontaneous polarization, $\bar{P}$, is often rather large ($10 - 100\,\mu\text{C}/\text{cm}^2$). Examples are $BiFeO_3$ ($T_{FE} \sim 1100\,\text{K}$, $T_N = 643\,\text{K}$) and $YMnO_3$ ($T_{FE} \sim 914\,\text{K}$, $T_N = 76\,\text{K}$) [2]. The second group, type-II multiferroics, consists in materials in which the magnetic and ferroelectric phases coexist and have the

same stability region. This leads to a strong coupling between the two orders, as the origin of one is dependent on the other (e.g. $TbMnO_3$ and $DyMnO_3$). In these cases, magnetism breaks spatial inversion, which allows the stabilization of ferroelectricity as a secondary order parameter. Because it is a secondary order parameter, the polarization in these materials is usually much smaller ($\sim 10^{-2}\,\mu C/cm^2$) [5].

In the beginning of this century, three events propelled the study of multiferroics. One was that theory began to treat the general problem of why the coexistence of magnetism and ferroelectricity is so rare [8], while the others were experimental achievements that identified the two distinct classes of multiferroics. In 2003, Ramesh's group successfully grew thin films of one of the few compounds that exhibit both polar and magnetic phases at room temperature, $BiFeO_3$, whose multiferroic properties in bulk are fairly weak but are greatly enhanced in thin-film form [9]. The second major experimental development, also in 2003, was the discovery by Tokura and Kimura in $TbMnO_3$ of a class of multiferroics where magnetism and ferroelectricity do not just coexist, but in which magnetism induces ferroelectricity [10]. Since then, the two perovskites have been extensively studied not only for their magnetoelectric performance but also for leading to new physics in the field of multiferroicity. A number of experimental findings and relevant physical models stemming from them have been proven to be broadly applicable to other multiferroics.

1.1 Orthorhombic Perovskites

Several multiferroics exhibit a crystallographic structure that stems from the ideal cubic perovskite of symmetry $Pm\bar{3}m$ (Fig.1.1.1 (a)) [11]. This structure has the general chemical formula ABX_3 and is one of the most well known structures for solid materials. The A-cation is usually a rare-earth (La to Lu) or a post-transition metal (Pb or Bi), the B-cation is a transition metal and the X anion is N, O or F. The ideal perovskite structure can be described as corner shared BX_6 octahedra, where the B cations occupy the corner-sharing octahedra centers and the A cations the dodecahedra centers. The BX_6 octahedra form chains along the cubic axes, with the A-cation occupying the dodecahedron cavity created by them. However, for the ideal cubic symmetry to be preserved, the ionic diameter of the A-cation must match the diagonals of the cavity between the BX_6 octahedra chains. This is often not the case and the perovskite structure becomes distorted. Considering the $12th$ coordination for the A cation and the $6th$ coordination for the B cation, this matching can be geometrically expressed by the Goldschmidt tolerance factor [12]:

$$t = \frac{r_A + r_X}{\sqrt{2}(r_B + r_X)}, \tag{1.1.1}$$

where r_A, r_B and r_X are the ionic radii of A, B and X, respectively. The ideal perovskite structure corresponds to $t = 1$ and is rarely observed, with $SrTiO_3$ and $CaTiO_3$ being the most remarkable cases, at least at room conditions [11]. For perovskite oxide compounds, ABO_3, where the A cation is a rare-earth, one typically has $t < 1$. Thus, the A cation

is small when compared to the cage of surrounding oxygens and, to optimize the A–O bond distances, a short-period cooperative rotation of the BO_6 octahedra takes place. The cubic symmetry is therefore lowered to a tetragonal, hexagonal (e.g. $YMnO_3$ and $HoMnO_3$) or orthorhombic one (e.g. $TbMnO_3$ and $DyMnO_3$) (Fig.1.1.1 (b)). Only the orthorhombic $Pbnm$ symmetry found on rare-earth manganites, $RMnO_3$ with R = La to Dy, and their solid solutions will be further discussed.

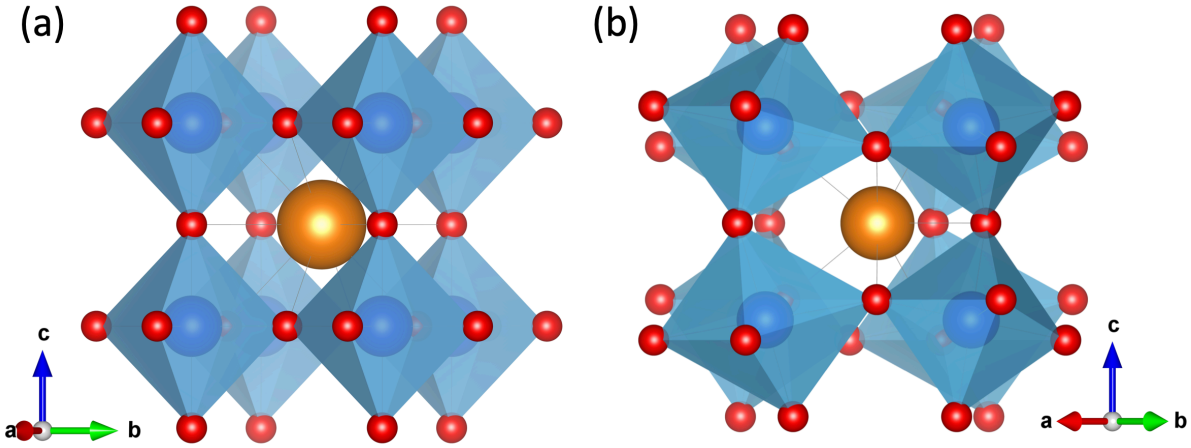

Figure 1.1.1: (a) Ideal cubic and (b) distorted perovskites with $Pm\bar{3}m$ and $Pbnm$ symmetries, respectively. The A and B cations are represented in orange and blue, respectively, while the O anion is in red. Made with $Vesta$ software.

The first order parameter symmetry-lowering distortions to the $Pbnm$ structure consist in in-phase and anti-phase tilts of the BO_6 octahedra, causing a fourfold increase of the primitive unit cell ($Z = 4$) [11, 13, 14]. The in-phase tilt occurs around the $[001]_{pc}$ and the anti-phase tilt around the $[110]_{pc}$ pseudocubic axes, with respect to the ideal $Pm\bar{3}m$ perovskite structure [11]. In Glazer's notation, the in-phase tilt about $[001]_{pc}$ is denoted by $a^0a^0c^+$, while the anti-phase tilt about the $[110]_{pc}$ axis is written as $a^-a^-a^0$ [11]. The coexistence of these tilts in the $Pbnm$ structure leads to the $a^-a^-c^+$ designation. It is important to stress that the presence of two anti-phase tilts, together with A cation displacements, imposes a deformation of the otherwise regular octahedra [15]. It is experimentally evidenced that, for the same B-cation, the magnitude of the tilt angles increases as the tolerance factor decreases, i.e., compounds with smaller rare-earth ions exhibit greater tilt angles [16].

In some cases, the octahedra can be further deformed whilst maintaining their $Pbnm$ symmetry due to the cooperative Jahn-Teller effect [17, 18]. The Jahn–Teller (JT) effect can be described by the JT theorem, essentially stating that any non-linear polyatomic system in a spatially degenerate electronic state spontaneously distorts. The distortion occurs in such a way that the degeneracy is lifted and a new equilibrium structure of lower symmetry is attained, lowering the overall energy of the system [17]. This effect is most often encountered in octahedral complexes of transition metals [19]. Such complexes distort along one of the molecular fourfold axes, which has the effect of removing the orbital

and electronic degeneracies and lowering the overall energy. In octahedral complexes, the JT effect is most pronounced when an odd number of electrons occupy the e_g orbitals [19]. This situation arises in complexes with the configurations d^9, low-spin d^7 or high-spin d^4, all of which have doubly degenerate ground states [19]. In such compounds, the e_g orbitals involved in the degeneracy point directly at the ligands, so that the distortion can result in a large energetic gain. The effect also occurs when there is a degeneracy due to the electrons in the t_{2g} orbitals, i.e., configurations such as d^1 or d^2 (both triply degenerate). However, the effect is much less noticeable because there is a much smaller lowering of repulsion on taking ligands further away from the t_{2g} orbitals, which do not point directly at the ligands. It should be stressed that in $RMnO_3$, as the Mn^{3+} ion has d^4 configuration, the JT effect wouldn't be present if just one electron was added (Fe^{3+} ion) or removed (Cr^{3+} ion). Also, the local distortions from the JT effect present a staggered long range order due to the also staggered orbital ordering on the ab-plane [18, 19].

All the aforementioned distortions can be tuned by chemical substitution and various external parameters such as temperature, stress and hydrostatic pressure. While chemical substitution of the A cation has been extensively studied, chemical substitution of the B cation has not. Regarding the latter, $RMnO_3$ and $RFeO_3$ are interesting candidates as they share the $Pbnm$ symmetry, as well as Wyckoff positions, and both Mn^{3+} and Fe^{3+} have the same ionic radii in the high-spin configuration. Yet, the latter is Jahn-Teller active while the former isn't. As will be seen in subsequent chapters, this can lead to the appearance of interesting physical properties in the solid solution $RMn_{1-x}Fe_xO_3$, with x ranging from 0 to 1 for a fixed R [20, 21, 22, 23].

1.2 Physical Properties of Orthorhombic Rare-Earth Manganites

In orthorhombic $RMnO_3$, the change in the ionic radius of the rare-earth, r_R, alters the balance between ferromagnetic (FM) and antiferromagnetic (AFM) superexchange interactions between Mn^{3+} ions through a change in the $Mn-O-Mn$ bond angles [24]. A $T-r_R$ phase diagram of orthorhombic $RMnO_3$ is displayed in Fig.1.2.1. An array of different magnetic phase sequences emerge as a function of r_R, allowing to tailor the physical properties of these compounds by changing the bond angle. It should be mentioned that, so far, the vast majority of the experimental results have been interpreted using models that, because the R-ions typically only order at temperatures below 10 K, neglect the $R-Mn$ and $R-R$ interactions [25].

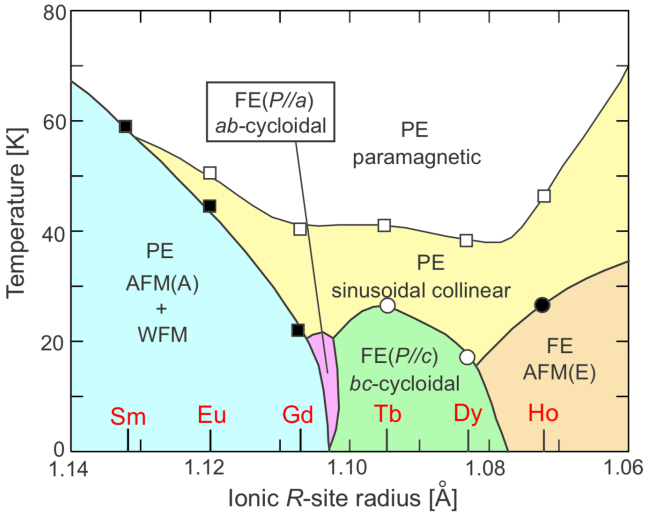

Figure 1.2.1: $T - r_R$ phase diagram of orthorhombic $RMnO_3$. The region between Gd and Tb was studied using a solid solution system $Gd_{1-x}Tb_xMnO_3$. Adapted from [24].

At high temperatures (~ 700 K, not shown in Fig.1.2.1), all compounds exhibit an orbital ordering transition associated with the stabilization of the Jahn-Teller distortion [15]. At room temperature, they are all paramagnetic and paraelectric [15]. In the last fifteen years, interesting magnetoelectric effects were reported in some of these compounds (R = Eu, Gd, Tb and Dy) [5, 26, 27]. For example, while $EuMnO_3$ has no spontaneous ferroelectric ground-state, a polarization along the a axis can be induced by applying a magnetic field along the b axis of 20 T [28]. Also, in $TbMnO_3$ and $DyMnO_3$, a ground state spiral spin order with concomitant ferroelectricity is stabilized below 28 K and 18 K, respectively. In 2004, Goto *et al.* showed that $TbMnO_3$ and $DyMnO_3$ exhibit a spontaneous electric polarization along the c axis [26] and, one year later, Kimura *et al.* published a detailed study of the magnetoelectric properties of these materials [5].

Regarding $TbMnO_3$, an incommensurate sinusoidal collinear order of the Mn^{3+} spins occurs below $T_N \approx 41$ K [29, 30]. In this phase, the spins are aligned along the b axis with a temperature dependent incommensurate propagation vector $\bar{q}_m \sim (0, 0.29, 1)$ at T_N [29, 30]. The structural modulation vector, $\bar{k}_l$, presents a similar behavior and is given by $\bar{k}_l = 2\bar{q}_m$. Below $T_c \approx 28$ K, the sinusoidal modulation turns into a cycloid spiral in the bc plane, as revealed by neutron diffraction studies [29, 30]. Upon further temperature decrease, ordering of the f electrons of the Tb ions takes place below $T_N^{Tb} \approx 7$ K [25]. The temperature dependence of the magnetization and inverse magnetic susceptibility, measured along each crystallographic axis and along the b and c axis of $TbMnO_3$, respectively, is depicted in Fig.1.2.2. The transitions at T_N, T_c and T_N^{Tb} are nicely seen through the anomalies in the temperature dependence of the magnetization/magnetic susceptibility measured along the c axis. It is also only along the c axis that a small splitting between the curves measured in zero-field cooling and field-cooling conditions below ~ 6 K is observed, hinting a weak ferromagnetic character of the magnetic phase. Also, the susceptibility, and hence the magnetization, measured along the a and b axes is considerably

larger than along the c axis, which is consistent with the latter being the hard magnetization axis. It can be seen in Fig.1.2.2 (b) that the inverse susceptibility starts to deviate significantly from the Curie–Weiss behavior below $\sim 200\,\mathrm{K}$, reaching a relative minimum around $120\,\mathrm{K}$ [31]. Even though several neutron diffraction studies were performed in this compound, none found a magnetic ordering other than the paramagnetic above $40\,\mathrm{K}$ [29, 30]. Thus, the origin of such peak remains an open question up to date.

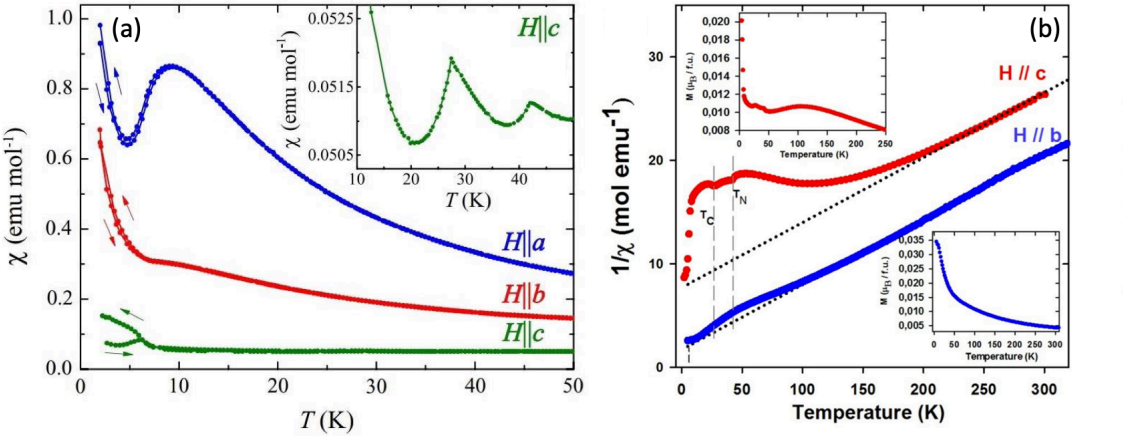

Figure 1.2.2: Temperature dependence of the (a) susceptibility and (b) inverse susceptibility, measured along each crystallographic axis and along the b and c axis of $TbMnO_3$, respectively. Adapted from [31].

A remarkable property of $TbMnO_3$ is that the emergence of a ferroelectric polarization coincides with the spin cycloid ordering below $T_c \sim 28\,\mathrm{K}$, implying an intrinsic entanglement between the spiral-type antiferromagnetism and ferroelectricity. The temperature dependence of the electric polarization of $TbMnO_3$ along the a, b and c axes for several magnetic fields applied along each crystallographic axis is depicted in Fig.1.2.3. Also, the temperature dependence of the electric polarization of $TbMnO_3$ along the c axis for even higher magnetic fields applied along each crystallographic axis is shown in Fig.1.2.4.

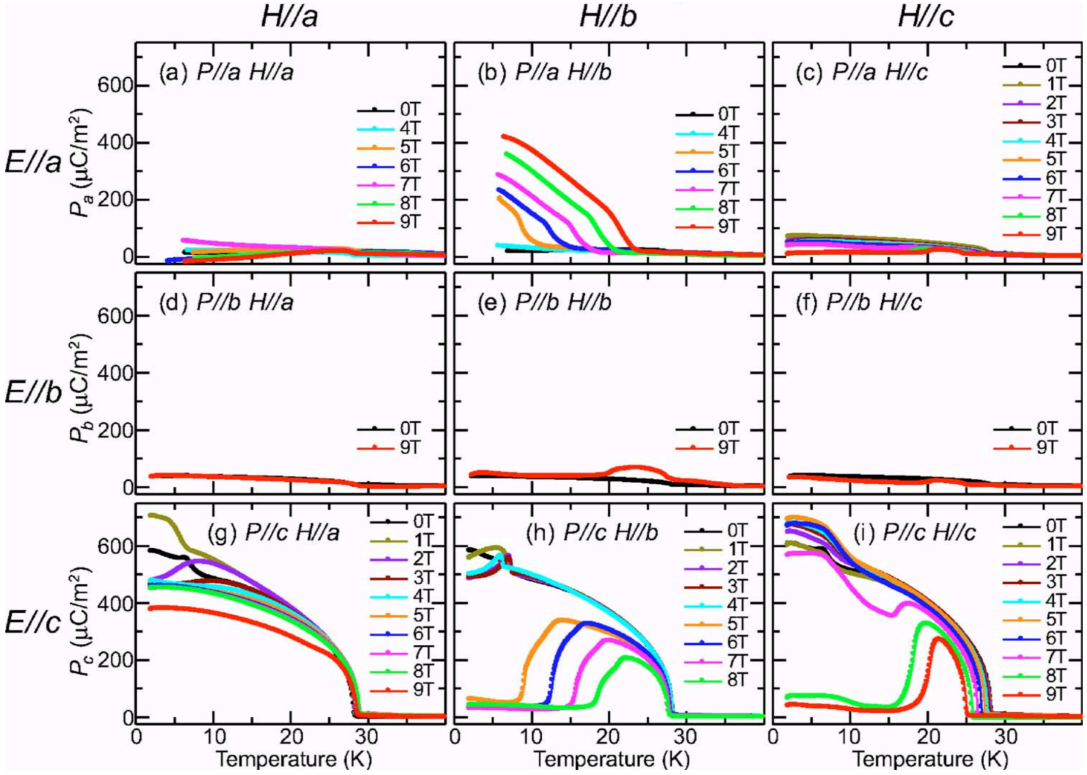

Figure 1.2.3: Temperature dependence of the electric polarization along the a, b and c axes for several magnetic fields (up to 9 T) applied along each crystallographic axis for $TbMnO_3$. Adapted from [5].

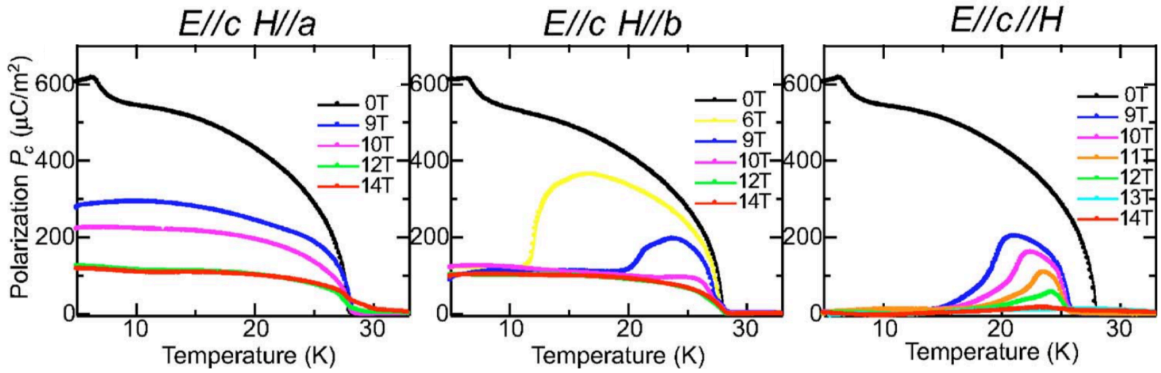

Figure 1.2.4: Temperature dependence of the electric polarization along the c axis for several high magnetic fields (9–14 T) applied along the (a) a, (b) b, and (c) c axes for $TbMnO_3$. Adapted from [5].

The onset temperature for the FE phase, $T_c \sim 28$ K, shows minimal magnetic field dependence. An interesting effect is observed for $B \parallel b$. While the polarization is roughly independent of B_b up to 4 T, a clear decrease in P_c is observed for higher fields. The temperature at which such decrease is noticeable, T_{flop}, increases with increasing magnetic field, being roughly equal to T_c for fields higher than 10 T (Fig.1.2.4). Furthermore, an increase in P_a is simultaneously observed at T_{flop}. Therefore, a switching of the polarization

from the c to the a axis occurs at T_{flop} for a magnetic field higher than 4 T applied along the b axis, further corroborating the strong coupling between magnetism and ferroelectricity [5]. For $B \parallel a$, the polarization along the c axis barely changes up to 8 T. However, P_c starts to decrease with higher magnetic fields already below T_c (Fig.1.2.4). Simultaneously, a polarization along the a axis appears below T_c. Therefore, a magnetic field along both the a and b axes causes the switching of the direction of $\vec{P}$ from the c to the a axis [5]. Interestingly, the effect of a high magnetic field along the c axis is different from along the other axes, as the polarization practically vanishes for all crystallographic directions and for all temperatures above 13 T (Fig.1.2.4). Thus, $TbMnO_3$ becomes non ferroelectric by applying a sufficiently large magnetic field along the c axis [5]. The aforementioned behaviors are summarized in the magnetoelectric phase diagrams for magnetic fields applied along the a, b and c axes shown in Fig.1.2.5.

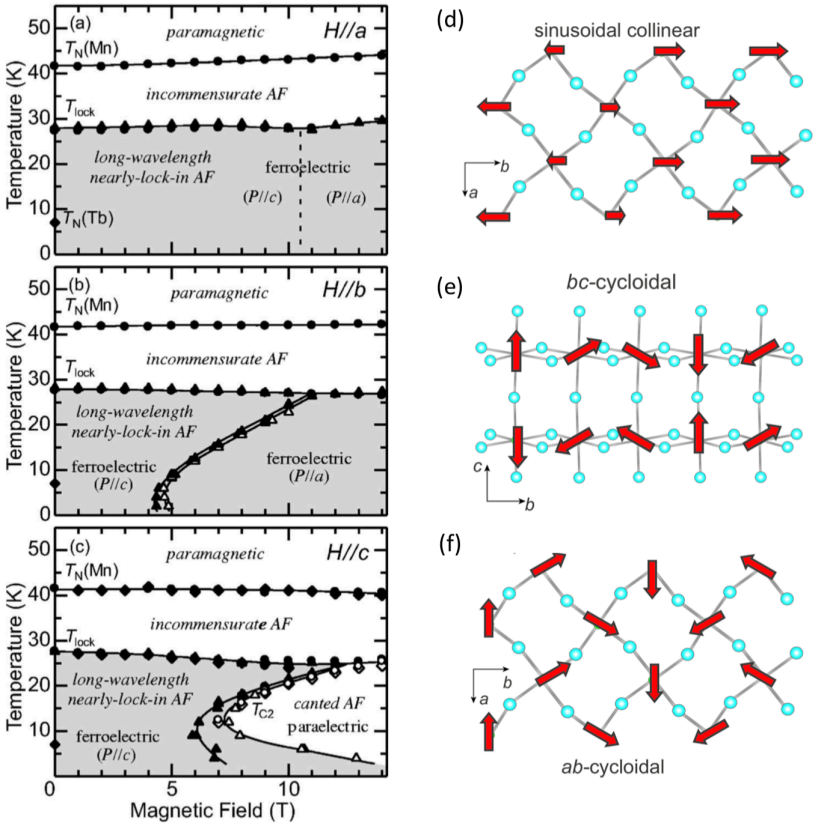

Figure 1.2.5: Magnetoelectric phase diagram of $TbMnO_3$ with magnetic fields applied along the (a) a, (b) b and (c) c axes. Spin configurations of the (d) sinusoidal collinear, (e) bc-cycloidal and (f) ab-cycloidal. Along the c axis, spins stack antiferromagnetically. Adapted from [5, 24].

Regarding the commensurability of the cycloidal and ferroelectric phase in $TbMnO_3$, it should be pointed out that contradictory results have been published. The temperature dependence of the b component of the modulation vector, $(0, q_m, 1)$, obtained independently through neutron diffraction by Kajimoto et al. and Kenzelmann et al. is shown

in Fig.1.2.6 [29, 30]. While Kajimoto et al. state that the modulation vector, $(0,\, q_m, 1)$, is temperature independent and commensurate below T_c, Kenzelmann et al. consider it to be temperature dependent, and thus, incommensurate [29, 30]. Furthermore, the data from both neutron diffraction experiments are quite similar. Also, in [5], the authors refer to q_m as being "nearly locked in" below $T_{lock} = T_c$, and thus, T_{lock} and T_c are interchangeably used to denote the temperature of the ferroelectric transition. It is the author's view that the modulation vector is incommensurate also below T_c, in accordance with the interpretation given by Kenzelmann et al. [30].

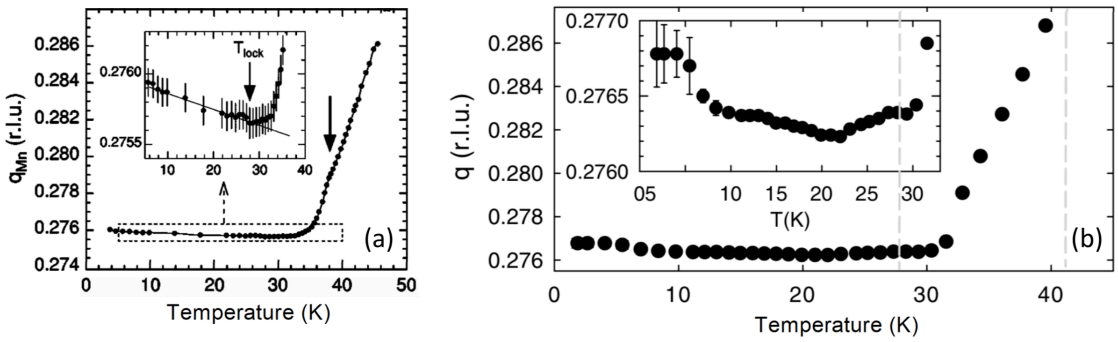

Figure 1.2.6: Temperature dependence of the b component of the modulation vector, $(0,\, q_m, 1)$, obtained through neutron diffraction by (a) Kajimoto et al. and (b) Kenzelmann et al. [29, 30].

Furthermore, it should be highlighted that the authors in [5] interpret the magnetic field induced switching of the polarization from the c to the a axis as being due to the rotation of the spin cycloidal from the bc to the ab plane. To understand why such connection makes sense and also gain more insight into some details of the physical mechanisms involved in $TbMnO_3$ and similar systems, two relevant theoretical models will be addressed in the following sections. Interestingly, neither model requires the assumption of a commensurate cycloidal phase, only that it is modulated.

1.3 Microscopic Model and Phase Diagrams of $RMnO_3$

In 2009, Mochizuki and Furukawa theoretically investigated the phase diagrams of $RMnO_3$ in the absence of external magnetic field [24]. The Mn $3d$ spin system is described through a classical $S = 2$ Heisenberg model with some additional interactions and magnetic anisotropies on a cubic lattice.

1.3.1 Model Hamiltonian

The Hamiltonian is considered to be [24]:

$$H = H_{exc} + H_{sia} + H_{DM} + H_{cub}. \tag{1.3.1}$$

The first term, H_{exc}, accounts for the superexchange interactions (depicted in Fig. 1.3.1). This term contains FM exchanges, J_{ab}, on the $Mn-Mn$ bonds along the cubic x and y axes and AFM exchanges, J_2, on the in-plane diagonal $Mn-Mn$ bonds along the b axis, as well as AFM exchanges, J_c, on the $Mn-Mn$ bonds along the c axis (see Fig.1.3.1). This term is given by [24]:

$$H_{exc} = -J_{ab} \sum_{<i,j>}^{x,y} \bar{S}_i \cdot \bar{S}_j + J_2 \sum_{<i,j>}^{b} \bar{S}_i \cdot \bar{S}_j + J_c \sum_{<i,j>}^{c} \bar{S}_i \cdot \bar{S}_j, \tag{1.3.2}$$

where the sum is over the nearest neighbors Mn^{3+} spins along the specified direction.

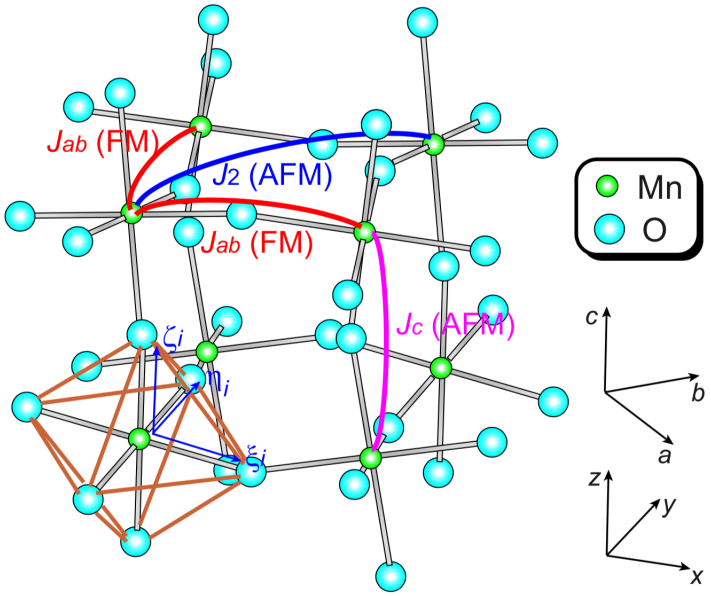

Figure 1.3.1: Superexchange interactions in $RMnO_3$ and tilted local coordinate axes ξ_i, η_i, and ζ_i attached to the ith MnO_6 octahedron. Ferromagnetic exchanges, J_{ab}, on the $Mn-Mn$ bonds along the cubic x and y axes, antiferromagnetic exchanges, J_2, along the orthorhombic b axis, and antiferromagnetic exchanges, J_c, along the c axis are considered. Adapted from [24].

Because of Jahn-Teller distortion in $RMnO_3$, the FM J_{ab} stems from the antiferro-arrangement of e_g orbitals in the ab-plane, while J_c is AFM due to the ferro-arrangement of the orbitals along the c axis. On the other hand, the AFM J_2 arises from an exchange path between two Mn e_g orbitals along the b axis via the $2p$ oxygen orbitals. The strength of the second-neighbor exchanges, J_2, increases with increasing octahedra tilting since this distortion enhances the hybridization between the two $2p$ oxygen orbitals. Owing to the frustration between J_{ab} and J_2, a spiral spin order is stabilized in some manganites, such as $TbMnO_3$, $DyMnO_3$ and also certain kinds of solid solutions [24].

The second term in the Hamiltonian (Eq.1.3.1), H_{sia}, represents the single-ion anisotropies, which are determined by the local environment of the Mn^{3+} ion surrounded by six oxygens. Letting ξ_i, η_i, and ζ_i denote tilted local coordinate axes attached to the ith MnO_6

octahedron, H_{sia} can be written as [24]:

$$H_{sia} = H_{sia}^{D} + H_{sia}^{E} = D\sum_{i} S_{\zeta_i}^2 + E\sum_{i}(-1)^{i_x+i_y}(S_{\xi_i}^2 - S_{\eta_i}^2), \tag{1.3.3}$$

where i_x, i_y, and i_z represent coordinates of ith Mn ion with respect to the cubic x, y, and z axes and D, E are constants. The H_{sia}^{D} term suggests that the ζ_i axis is a local hard magnetization axis at every site, making the c axis a hard magnetization axis. On the other hand, due to the staggered ordering of the occupied e_g orbitals, H_{sia}^{E} implies that the ξ_i and η_i axes are local hard magnetization axes alternately in the ab-plane.

The third term, H_{DM}, denotes the Dzyaloshinsky-Moriya (DM) interaction and is given by [24]:

$$H_{DM} = \sum_{<i,j>} \bar{D}_{ij} \cdot (\bar{S}_i \times \bar{S}_j). \tag{1.3.4}$$

The DM interaction will be discussed in greater detail in a subsequent section. Because of crystal symmetry, the DM vectors can be written as [24]:

$$\bar{D}_{ij}^{x} = (-1)^{i_x+i_y+i_z}(\alpha_{ab},\, -\beta_{ab},\, (-1)^{-i_z}\gamma_{ab}) \tag{1.3.5}$$

$$\bar{D}_{ij}^{y} = (-1)^{i_x+i_y+i_z}(-\alpha_{ab},\, -\beta_{ab},\, (-1)^{-i_z}\gamma_{ab}) \tag{1.3.6}$$

$$\bar{D}_{ij}^{z} = -(-1)^{i_z}(\alpha_c,\, (-1)^{i_x+i_y}\beta_c,\, 0), \tag{1.3.7}$$

where $\bar{D}_{ij}^{k}$ stands for the DM vector along the $Mn_i - O - Mn_j$ bond in the positive k direction ($k = x,\, y,\, z$) and α_{ab}, β_{ab}, γ_{ab}, α_c, β_c are constants.

The last term, H_{cub}, merely represents the cubic anisotropy, originating from the nearly cubic symmetry of the perovskite lattice [24]:

$$H_{cub} = \frac{a}{S(S+1)}\sum_{i}(S_{x_i}^4 + S_{y_i}^4 + S_{z_i}^4), \tag{1.3.8}$$

where a is a constant. Details on the values of all the parameters previously mentioned and how they were obtained can be found elsewhere [24].

One of the main outcomes of this model is the explanation in terms of the single-ion anisotropies and the DM interaction of why the spin cycloidal lies in the bc plane rather than the ab plane. As this is fundamental to understand the physical behavior of these compounds, that result is explored in the next section.

1.3.2 Why the bc-cycloidal spin state?

In $RMnO_3$, the c axis is always a hard magnetization axis due to the single-ion anisotropies, H_{sia}^{D}. Therefore, at first sight, the bc-cycloidal spin state should be higher in energy than

the ab-cycloidal spin state, making the emergence of the bc-cycloidal spin order intriguing. Furthermore, the bc-cycloidal spin phase emerges right next to the ab-cycloidal spin phase with increasing octahedral tilting (see Fig.1.2.1).

If the Hamiltonian only contained the superexchange term, spins in the cycloidal state would rotate uniformly. The angle between adjacent spins along the x or y axes, ϕ_{ab}, is given by [24]:

$$cos\phi_{ab} = \frac{J_{ab}}{2J_2} \tag{1.3.9}$$

while the angle between adjacent spins along the c axis is $\phi_c = \pi$ due to the strong AFM exchange J_c. However, when DM interactions are taken into account, a modulation of those angles occurs. In the ab-cycloidal spin state, the rotating spins couple dominantly to the c components of the DM vectors on the in-plane $Mn-O-Mn$ bonds (Eq.1.3.4), wherein their magnitudes are all equal to γ_{ab} and their signs alternate along the x and y bonds [24]. The rotation angles then become alternately modulated into $\phi_{ab} \pm \Delta\phi_{ab}$, with $\Delta\phi_{ab} > 0$ (Fig.1.3.2 (a)). The energy gain per bond due to this angle modulation can be written as [24]:

$$\Delta E^{ab}_{DM} = -\gamma_{ab}S^2|sin(\phi_{ab} \pm \Delta\phi_{ab}) - sin(\phi_{ab})| \approx -\gamma_{ab}S^2|cos(\phi_{ab})|\Delta\phi_{ab}. \tag{1.3.10}$$

Because the energy gain $|\Delta E^{ab}_{DM}|$ decreases with increasing ϕ_{ab}, it becomes clear from (Eq.1.3.9) that the ab-cycloidal spin state becomes less energetically favorable with increasing J_2 or, equivalently, increasing octahedral tilting.

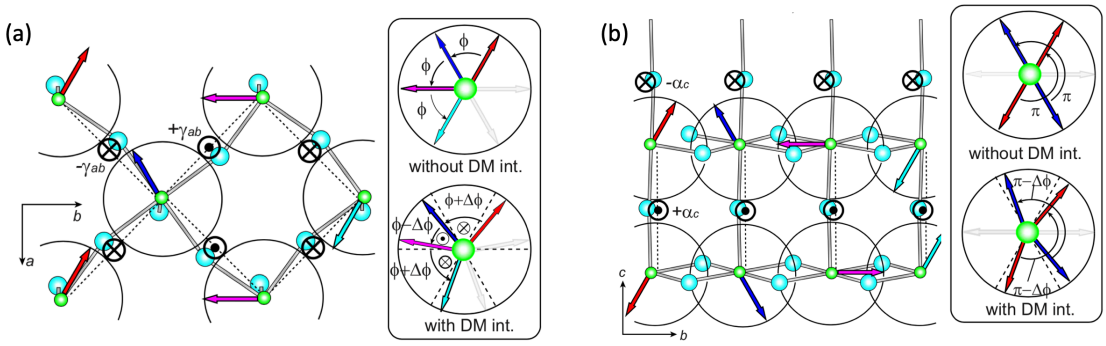

Figure 1.3.2: (a) ((b)) Spin structure in the ab-cycloidal (bc-cycloidal) state and arrangement of the c (a) components of DM vectors on the in-plane (out-of-plane) $Mn-O-Mn$ bonds. The panel on the right (left) side illustrates spin directions in the ab-cycloidal and (bc-cycloidal) states with uniform rotation angles in the absence of DM interactions and with modulated rotation angles in the presence of DM interactions. Adapted from [24].

Furthermore, spins in the bc-cycloidal spin state couple predominantly to the a components of the DM vectors on the out-of-plane $Mn-O-Mn$ bonds (Eq.1.3.4). Their magnitudes are all equal to α_c and their signs are the same within a plane but alternate

along the c axis (Fig.1.3.2 (b)). Similarly, recalling that $\phi_c = \pi$ due to the strong AFM exchange J_c ,the energy gain per bond is now given by [24]:

$$\Delta E_{DM}^{bc} = -\alpha_c S^2 |sin(\phi_c \pm \Delta\phi_c) - sin(\phi_c)| \approx -\alpha_c S^2 \Delta\phi_c \tag{1.3.11}$$

Thus, $|\Delta E_{DM}^{bc}|$ is independent of J_2 and the energetic advantage of the bc-cycloidal spin state relative to the ab-cycloidal one, $|\Delta E_{DM}^{bc} - \Delta E_{DM}^{ab}|$, is owed to the DM interactions and increases as J_2 increases. Then, it becomes clear that the bc-cycloidal spin state is preferred when the energy gain from the DM interactions dominates over the energetic disadvantage due to the hard magnetization c axis. In [24], the authors obtained $T - J_2$ phase diagrams for several values of α_c (depicted in Fig.1.3.3), showing that the region of stability of the bc-cycloidal phase increases with increasing α_c.

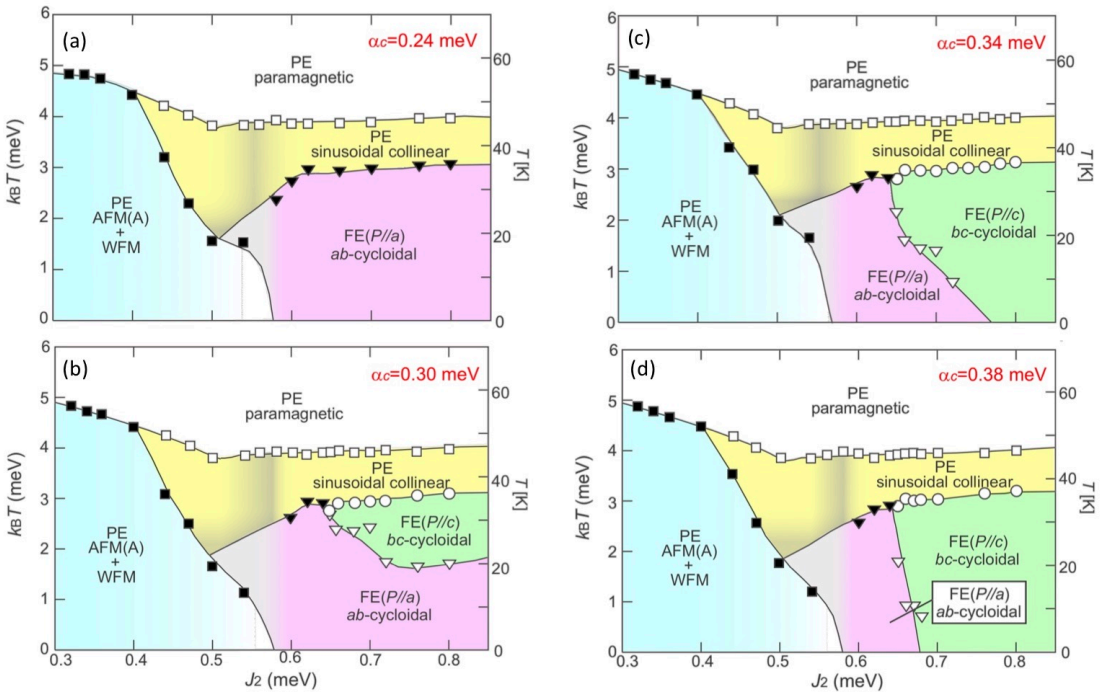

Figure 1.3.3: Theoretically obtained phase diagrams for (a) $\alpha_c = 0.24$ meV, (b) $\alpha_c = 0.30$ meV, (c) $\alpha_c = 0.34$ meV, and (d) $\alpha_c = 0.38$ meV where α_c is the magnitude of the a component of the DM vector on the out-of-plane $Mn - O - Mn$ bond. PE and FE denote paraelectric and ferroelectric phases, respectively. Also, $AFM(A) + WFM$ denotes the A-type AFM phase with weak FM due to spin canting. Adapted from [24].

In conclusion, the relative stability of the ab- and bc-cycloidal spin states in $RMnO_3$ is owed to a balance between the single-ion anisotropies and the DM interactions. Namely, the hard magnetization c axis due to the single-ion anisotropy favors the stability of the ab-cycloidal state, while the bc-cycloidal state is stabilized by the DM vectors on the out-of-plane bonds.

Even though this model provides explanation for several key features of the magnetic structure of orthorhombic rare-earth manganites, it lacks two important pieces. Firstly, up

to the time of writing, it has not been extended to explain the interesting effects of an applied magnetic field along one of the crystal axes. Secondly, it was simply assumed that in the cycloidal phase there is some mechanism that induces a ferroelectric polarization perpendicular to both the cycloidal's propagation vector and the spin's helicity, not pursuing the matter any further [24]. However, Sergienko and Dagotto developed a model based on the DM interaction that aims at explaining the appearance of a ferroelectric polarization in the spin cycloidal phase [32]. Interestingly, the authors did not regard how such structure stabilizes in the first place. Therefore, the next section will be devoted to presenting the Sergienko-Dagotto model and showing how it connects with the one by Mochizuki and Furukawa.

1.4 Sergienko-Dagotto Model

After understanding the phase sequence in $TbMnO_3$, one may wonder what mechanism lies behind the appearance of a polarization in the bc-cycloidal spin phase. Starting from the known magnetic structure of $TbMnO_3$, the model proposed by Sergienko and Dagotto shows how it leads to the emergence of ferroelectricity [32]. In an ABO_3 perovskite with ideal cubic structure, the B–O–B bonds are linear (180^o bond angle) and have rotational symmetry with respect to their B–B axis. Due to the size mismatch between the A and B ions, the oxygen octahedra tilt and rotate. Therefore, each oxygen ion between two neighboring B ions may move away from the middle point, resulting in a bent B–O–B bond and the B–B axis rotational symmetry breaking [6]. The bent B–O–B bond will then induce the DM interaction as a relativistic correction to the superexchange between magnetic B ions in the presence of spin–orbit coupling [33]. As in the previous section, the DM Hamiltonian can be expressed as:

$$H_{DM} = \sum_{<i,j>} \bar{D}_{ij} \cdot (\bar{S}_i \times \bar{S}_j), \tag{1.4.1}$$

where the vector $\bar{D}_{ij}$ is constricted by symmetry and, for a perovskite structure with bent B–O–B bonds, it must be perpendicular to the B_i–O–B_j plane. In a first approximation, the magnitude of $\bar{D}_{ij}$ is proportional to the displacement of the oxygen ion from its position in the ideal perovskite structure, $\bar{d}_i$:

$$\bar{D}_{ij} = \gamma \hat{e}_{ij} \times \bar{d}_i \tag{1.4.2}$$

where $\hat{e}_{ij}$ is the unit vector pointing from the B_i-site to the B_j-site and γ is a constant. In an ideal cubic perovskite, $\bar{D}_{ij} = 0$. However, in a distorted perovskite structure with lower symmetry, the cooperative tilting of the oxygen octahedra leads to a reversal of the direction of $\bar{D}_{ij}$ between the nearest-neighbor B–O–B bonds (Fig.1.4.1) if all the O–B–O (not B–O–B) bond angles are 180^o (i.e. rigid octahedra).

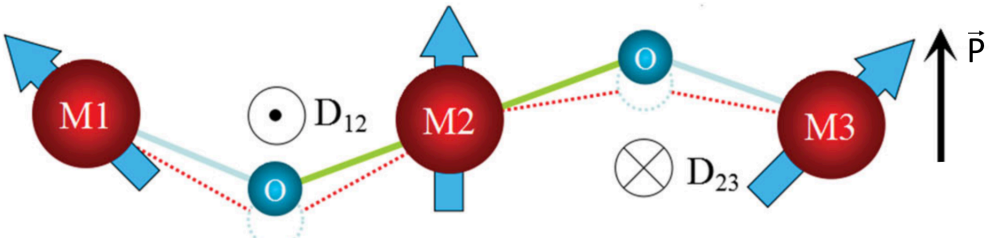

Figure 1.4.1: Rotational symmetry along the B_i–O–B_j axis is broken due to bond bending. The asymmetric DM interaction is allowed, with the $\bar{D}_{ij}$ vector orthogonal to both the B_i–O–B_j axis and the oxygen's displacement vector. A noncollinear spin pattern with a fixed helicity will uniformly modulate the DM vector to lower the energy, generating aligned ferroelectric dipoles. Adapted from [6].

In this case, the Hamiltonian can be written as [32]:

$$H = H_{DM} + H_{el} = \sum_i \left[\gamma(\hat{e}_{i,i+1} \times \bar{d}_i) \cdot (\bar{S}_i \times \bar{S}_{i+1}) + \frac{\kappa}{2} d_i^2\right] \equiv \sum_i H_i, \tag{1.4.3}$$

where H_{el} is the elastic energy and κ is the stiffness [32]. Considering, for example, a chain of B-atoms along the x-axis,

$$\hat{e}_{i,i+1} \times \bar{d}_i = \hat{x} \times (d_{x_i}, d_{y_i}, d_{z_i}) = d_{y_i}\hat{z} - d_{z_i}\hat{y}. \tag{1.4.4}$$

Then, the displacement, $\bar{d}_i$, that minimizes H_i is:

$$\bar{d}_i = \frac{\gamma}{\kappa}(0, -(\bar{S}_i \times \bar{S}_{i+1}) \cdot \hat{z}, (\bar{S}_i \times \bar{S}_{i+1}) \cdot \hat{y}) = \frac{\gamma}{\kappa}\hat{x} \times (\bar{S}_i \times \bar{S}_{i+1}). \tag{1.4.5}$$

Or, generalizing the previous equation to a chain of B-atoms along any direction,

$$\bar{d}_i = \frac{\gamma}{\kappa}\hat{e}_{i,i+1} \times (\bar{S}_i \times \bar{S}_{i+1}) \tag{1.4.6}$$

Since in a spiral magnet with fixed helicity $\bar{S}_i \times \bar{S}_{i+1}$ points uniformly in one direction, all the induced ionic displacements are along the same direction. This gives rise to a macroscopic ferroelectric polarization as a sum of local polarizations in the direction perpendicular to the spiral's helicity and propagation vector [32]:

$$\bar{P} \propto \sum_i \hat{e}_{i,i+1} \times (\bar{S}_i \times \bar{S}_{i+1}) \tag{1.4.7}$$

In fact, $TbMnO_3$ exhibits a cycloid spiral spin order in the bc plane with the propagation vector along the b-axis below 28 K. Thus, the induced polarization ($\propto \hat{e}_{ij} \times (\bar{S}_i \times \bar{S}_j)$) should lie along the c-axis, which is in agreement with experiment. Also, it was observed in $TbMnO_3$ and $DyMnO_3$ that an applied magnetic field can switch the polarization from the c to the a axis [5]. Thus, within this model it is possible to attribute such polariza-

tion switching to the rotation of the spin cycloidal from the bc to the ab plane. It then becomes clear that the model by Mochizuki and Furukawa and the one by Sergienko and Dagotto complement each other, as the first provides insight into the magnetic structure of orthorhombic rare earth manganites and the second into the polar character of the spin cycloidal phase. Interestingly, the Sergienko-Dagotto Hamiltonian is contained in the Hamiltonian in Eq.1.3.1. Nonetheless, it should be stressed that there are other models that arrive at Eq.1.4.7 through very different physical considerations.

1.4.1 Besides the Sergienko-Dagotto Model

Besides the previously mentioned ionic displacements, the spin–orbit coupling may distort the electron cloud surrounding an ionic core for a noncollinear spin pair, leading to a pure electronic charge dipole. Katsura, Nagaosa, and Balatsky approached this issue through perturbation theory on the Hubbard model with spin–orbit coupling (KNB theory), showing that the induced charge dipole is proportional to $\hat{e}_{i,i+1} \times (\bar{S}_i \times \bar{S}_{i+1})$ [34]. No ionic displacement contribution was considered and this theory can be viewed as a counterpart of the Sergienko–Dagotto model. While the latter is based on the ionic shift and the former on the electronic bias, both mechanisms may contribute to the total polarization. Nevertheless, density functional calculations suggest that the contribution from the ionic displacements is dominant in $TbMnO_3$ [35, 36], as confirmed experimentally [37].

1.5 Electromagnons in $RMnO_3$

The coexistence of magnetic and ferroelectric phases in multiferroic materials gives rise to important effects associated with the cross correlation between order parameters and external fields [5, 10]. Remarkably, it can happen that the elementary excitations are not purely magnetic nor ferroelectric in nature. Spin waves can be coupled with the electric polarization related optical lattice modes, giving rise to electric dipole active magnons, the so-called *electromagnons* [38]. Electromagnons were postulated in 1969 by Baryakhtar and Chupis [39, 40] but their existence was only experimentally verified in 2006 by Pimenov et al. in $TbMnO_3$ and $GdMnO_3$ through THz time-domain spectroscopy [41].

Figure1.5.1 shows the spectra of the imaginary part of the electric permittivity, ϵ'', in all the light polarization configurations for $TbMnO_3$ in the $15 - 80\,\mathrm{cm}^{-1}$ range [42]. The clear enhancement of ϵ'' is observed for $E^\omega \parallel a$ in the cycloidal phase, regardless of the direction of the magnetic component of the incident radiation. Thus, those excitations around 20 and $60\,\mathrm{cm}^{-1}$ are electrically active and are identified as electromagnons. Only the lowest energy peak around $20\,\mathrm{cm}^{-1}$ was reported by Pimenov et al. due to a shorter available spectral range [41]. A small peak is observed in the $(E^\omega \parallel b,\, H^\omega \parallel c)$ configuration around $20\,\mathrm{cm}^{-1}$ at $12\,\mathrm{K}$. Since this absorption peak is only active for $H^\omega \parallel c$, i.e., not observed in the $(E^\omega \parallel b,\, H^\omega \parallel a)$ configuration, it is assigned to the conventional

one-magnon AFM resonance [42]. Thus, apart from the weak one-magnon absorption, the intense absorption band arises only for $E^{\omega} \parallel a$, irrespectively of the direction of H^{ω}.

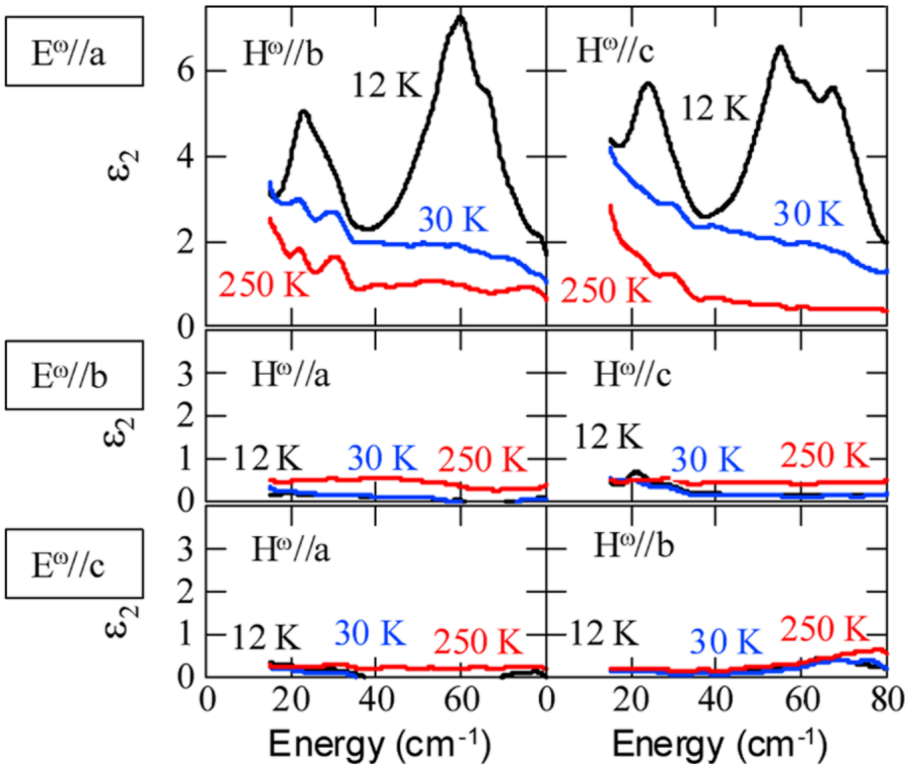

Figure 1.5.1: ϵ'' spectra of $TbMnO_3$ measured at 12, 30 and 250 K in all the crystallographically independent light polarization configurations. The temperatures of 250, 30 and 12 K correspond to the paramagnetic, collinear sinusoidal and bc-spiral phase, respectively. E^{ω} and H^{ω} denote the electric and magnetic fields of light, respectively. Taken from [42].

The temperature dependence of the ϵ'' spectra up to $180\,\mathrm{cm}^{-1}$ for $E^{\omega} \parallel a$ is shown in Fig.1.5.2. Below $80\,\mathrm{cm}^{-1}$ (region I), a flat broad band is discerned in the collinear sinusoidal phase at 30 and 40 K. Below 28 K, in the cycloidal phase, a two-peak structure appears in the $20 - 80\,\mathrm{cm}^{-1}$ region and its intensity rapidly evolves on cooling. In [42], the authors refer to both electromagnons as a whole, calling it the $2M$ excitation. In the $93 - 122\,\mathrm{cm}^{-1}$ energy range (region II), where the spectra are dominated by an optical phonon mode, both the spectral intensity and peak position show significant temperature dependence. A sharp decrease of intensity with decreasing temperature is clearly observed, suggesting a strong coupling of this phonon with the $2M$ excitation [42].

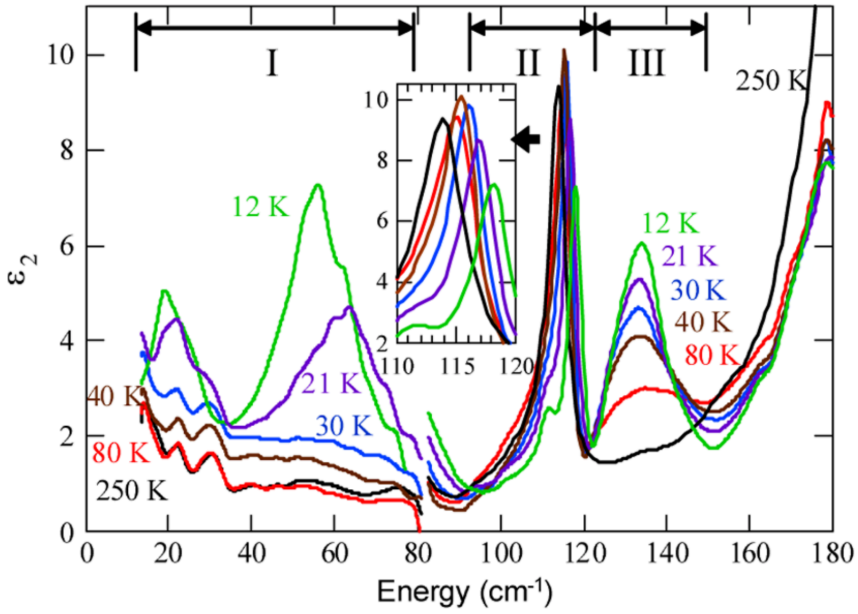

Figure 1.5.2: Temperature dependence of the ϵ'' spectra for $E^{\omega} \parallel a$ in $TbMnO_3$. Three energy ranges are indicated as I, II, and III. The inset shows the changes in frequency and intensity of the phonon located between 110 and $120\,\mathrm{cm}^{-1}$ (region II). Taken from [42].

To ascertain this apparent coupling with a phonon, Takahashi et al. calculated the integrated spectral weight per Mn site, defined as [42]:

$$N_{eff} = \frac{2m_0 V}{\pi e^2} \int_{\omega_1}^{\omega_2} \omega \epsilon''(\omega) d\omega, \tag{1.5.1}$$

where m_0, e, and V are the free electron mass, electric charge and unit-cell volume, respectively. All quantities in Eq.1.5.1 are calculated at a fixed temperature. However, there are no published studies regarding the temperature dependence of the lattice parameters of $TbMnO_3$. Because the temperature dependence of N_{eff} is most important at low temperatures, volume variations in the $10 - 250\,\mathrm{K}$ temperature range are assumed be irrelevant. Three regions of integration were considered (regions I, II and III shown in Fig.1.5.2). In Fig.1.5.3, the temperature dependence of $\Delta N_{eff}(T) \equiv N_{eff}(T) - N_{eff}(T = 250\,\mathrm{K})$ is depicted for each of those regions.

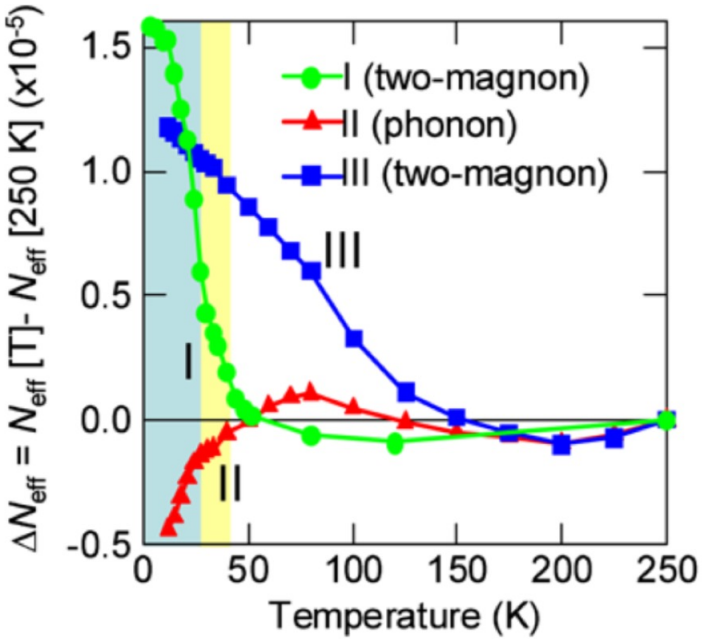

Figure 1.5.3: Temperature dependence of ΔN_{eff} in the I, II and III energy regions for $TbMnO_3$. The yellow and blue regions denote the sinusoidal collinear and cycloid phases, respectively. Adapted from [42].

The slight decline of N_{eff} below $250\,\mathrm{K}$ in all regions is attributed to the change of the absorption tail arising from higher-energy phonons [42]. This variation is, however, negligible if compared with the substantial changes observed at low temperatures. On further temperature decreasing, the intensity in region III increases from $150\,\mathrm{K}$, a much higher temperature than T_N ($41\,\mathrm{K}$), being ascribed to the anisotropic development of short-range spin order well above T_N [42]. In contrast, the low-energy side (region I) shows a rapid build-up from T_N and the rate at which its intensity increases becomes higher in the cycloidal phase. In region II, N_{eff} starts to decrease below $80\,\mathrm{K}$ and such decrease becomes much steeper in the cycloidal phase. This indicates that the lowest-lying optical phonon mode is strongly coupled with the $2M$ excitation [42]. However, the increase of the oscillator strength in regions I and III at $12\,\mathrm{K}$ is 6 times larger than the decrease of that of region II. Thus, in the light of the sum rule, the $2M$ spectral weight comes not only from the nearby optical phonon, but maybe also from higher energy phonons and/or other electronic excitations [42].

Regarding the observed $E^{\omega} \parallel a$ selection rule in $TbMnO_3$, it was shown that it also applies to $DyMnO_3$ and $GdMnO_3$ [43, 44]. Because the DM interaction is one of the key mechanisms behind ferroelectricity in these materials, it was expected that it could also be essential to the existence of electromagnons. Katsura et al. showed that the collective excitation directly reflecting the DM mechanism is the electric field driven rotation mode of the spiral plane, interpreting the first experimental observations of the THz optical spectra in $RMnO_3$ ($R = \mathrm{Tb}, \mathrm{Dy}, \mathrm{Gd}$) as being do to that collective excitation associated with fluctuations of the polarization's direction [45]. This magnon mode should only be active when

the electric field of light, E^{ω}, is perpendicular to the spin spiral plane [45]. However, when THz time-domain spectroscopy experiments were carried out in $Eu_{1-x}Y_xMnO_3$, whose spin spiral lies in the ab plane ($P \parallel a$), it was found that the electromagnon selection rule remained $E^{\omega} \parallel a$ instead of becoming $E^{\omega} \parallel c$ [46]. The same behavior was observed in the magnetic field induced $P \parallel a$ phase in both $DyMnO_3$ and $TbMnO_3$ [43, 47]. Thus, the DM interaction is ruled out[1] as the origin of the observed strong electromagnon resonances, paving the way to the pursuit of other physical mechanisms.

Another puzzling experimental observation is that in some compounds the lower-energy electromagnon, unlike the higher-energy one, is also well defined in the collinear sinusoidal phase. This is observed, e.g., in $DyMnO_3$ (Fig.1.5.4) [43], $Gd_{0.7}Tb_{0.3}MnO_3$ [48], and $Eu_{1-x}Y_xMnO_3$ [49].

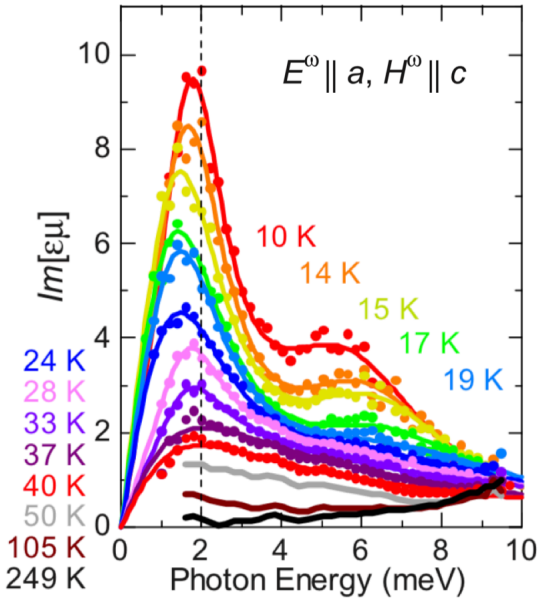

Figure 1.5.4: Temperature dependence of the imaginary part of the $\epsilon\mu$ spectra of $DyMnO_3$. Adapted from [43].

Apart from its fundamental importance, the electromagnon spectra can provide invaluable information on how magnetism couples to ferroelectricity [38]. Contrary to predictions based on DM coupling, electromagnons in $RMnO_3$ are observed only when the electric field of light is along the crystallographic a direction [43, 50, 51, 52]. Moreover, for all R ions considered, two electromagnons are always observed. The origin of one of those electromagnons was explained by Aguilar et al., who pointed out that the high-frequency electromagnon is a zone-edge magnon activated by pure magnetostriction [43, 50]. However, the origin of the low-frequency electromagnon remains under debate. Two quite different models were proposed for its explanation. Stenberg and de Sousa showed that magnetostriction along with spin-orbit coupling is able to explain the origin of both electro-

[1] A weak electromagnon resonance consistent with the DM model was observed in $TbMnO_3$ under applied magnetic field [47].

magnons even when the cycloid ground state is purely harmonic [38]. On the other hand, Mochizuki, Furukawa, and Nagaosa showed that pure magnetostriction along with cycloid anharmonicity created by single-ion anisotropy and a biquadratic spin interaction are able to explain the two electromagnons of the cycloid phase, implying that anharmonicity plays a vital role [53]. However, while the former is not able to explain the optical activity of the low-energy electromagnon in the sinusoidal phase, the latter was later extended to explain such observations [54].

1.6 B-site substitution in $TbMnO_3$

The discovery of the experimental phase diagram as a function of the tilt angle for $RMnO_3$ [55] and subsequent theoretical explanation [24], paved the way for chemical substitution studies on these compounds. As previously mentioned, the balance between competing exchange interactions depends on the $B-O-B$ angle. Thus, to explore the delicate coupling between magnetism and structure, several authors have been dedicated to changing the structure, in a controlled way, through chemical substitution [55, 56, 57, 58]. While A-site substitution is associated with tilting, B-site substitution implies a change in the octahedra distortion and dimensions, as well as in the magnetic and transport properties. Therefore, in B-site substitution, both structural distortions and magnetic properties are simultaneously changed. Because in $RMnO_3$ the B-site cation is Jahn-Teller active, chemical substitution on that site by non-active Jahn-Teller cations will modify the amplitude of the octahedra distortions and its asymmetry. Even though B-site substitution in these compounds can be easily achieved using different transition metal cations, the most suitable choice is Fe^{3+} as it has the same ionic radius as Mn^{3+} (0.645 Å in the high spin configuration and $6th$ coordination), reducing the number of varying parameters [59].

In 2016, three different works focused on identifying the magnetic structures and transitions of $TbMn_{1-x}Fe_xO_3$ through neutron diffraction [57, 60, 61]. It was found that, similarly to $DyMn_{1-x}Fe_xO_3$, the cycloidal magnetic ordering is already absent for $x = 0.1$ [56, 57]. Even though several interesting magnetic phases were ascertained, no connection to the multiferroic properties of $TbMnO_3$ was made whatsoever. One year later, Vilarinho et al. published a set of experimental results regarding $TbMn_{1-x}Fe_xO_3$ ceramics in the whole concentration range ($0 \leq x \leq 1$), that led to proposing the (x, T) magnetic phase diagram shown in Fig.1.6.1 [20, 21].

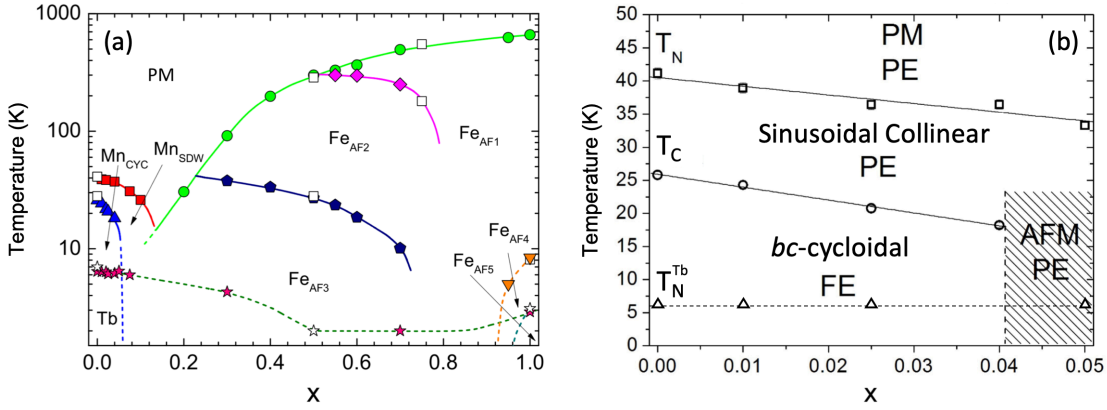

Figure 1.6.1: (x, T) magnetic phase diagram of the $TbMn_{1-x}Fe_xO_3$ system for (a) the whole concentration range and (b) for $x < 0.05$. The dotted lines mark the magnetic ordering of the Tb^{3+} ions. In panel (b), the gray area is a guess for the AFM and paraelectric phase. Adapted from [20, 21].

From Fig.1.6.1 (a), it becomes clear that the presence of Fe^{3+} strongly affects both the phase sequence and the magnetic structures. However, the scope of this dissertation lies in the multiferroic properties of the solid solution, which is why only the $x < 0.05$ concentration range will be further discussed. As it was already known that the multiferroic properties were absent for $x = 0.1$, the $TbMn_{1-x}Fe_xO_3$ ceramics with small Fe^{3+} concentrations were thoroughly studied to unravel the evolution of the multiferroic and magnetoelectric properties as a function of x, temperature and applied magnetic field [21]. The temperature dependence of the specific heat divided by temperature, C/T, as well as the real, ϵ', and imaginary, ϵ'' parts of the electric permittivity are depicted in Fig.1.6.2. Due to the resemblance of the temperature dependence of C/T and ϵ' between $TbMnO_3$ and the compounds with $x \leq 0.04$, the phase sequence was assumed to be the same [21]. Furthermore, while both T_N and T_c decrease with increasing x, T_N^{Tb} barely shifts with x. For Fe^{3+} concentrations above 4%, the anomaly associated with T_c is no longer perceived in the permittivity and specific heat curves, being interpreted as the suppression of the cycloidal spin ordered phase for $x > 0.04$.

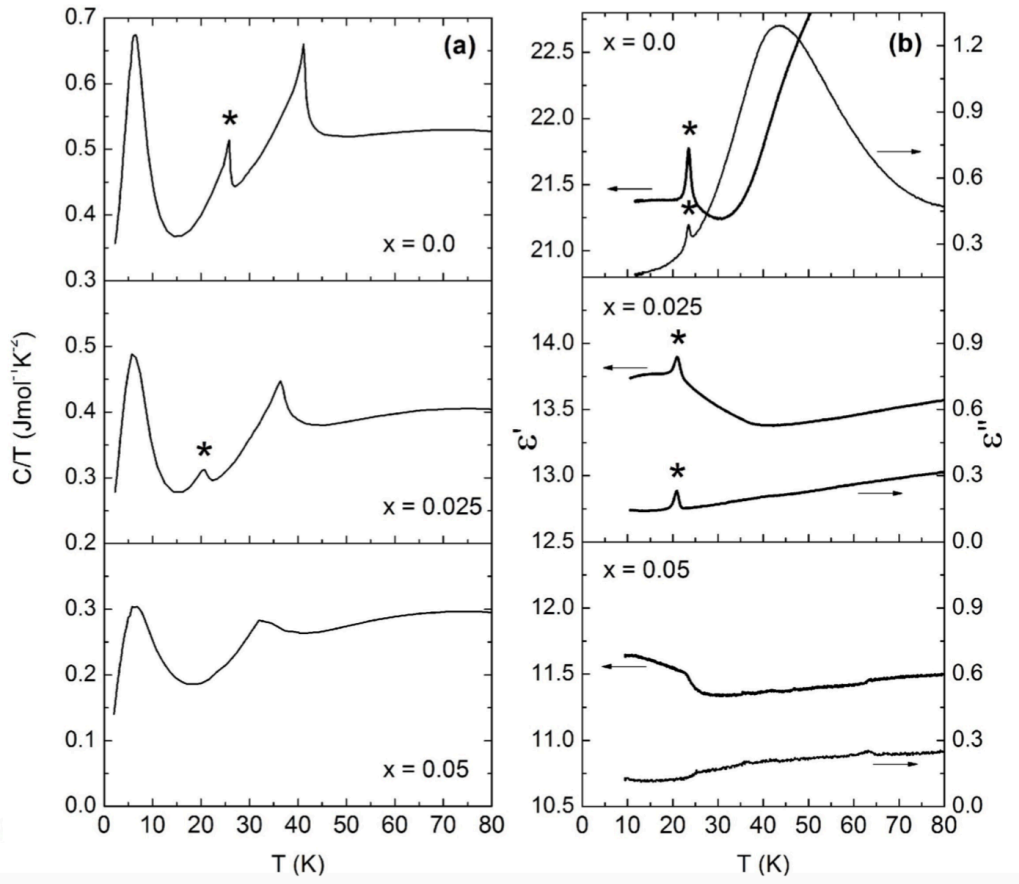

Figure 1.6.2: (a) Specific heat divided by temperature and (b) real and imaginary parts of the electric permittivity, measured in heating runs at 85.7 kHz, for x $= 0.0,\ 0.025$ and 0.05. Star ($*$) marks T_c, the temperature of the ferroelectric phase transition. Taken from [21].

To gain further insight in to the effect of Mn^{3+} substitution by Fe^{3+} on the multiferroicity of these compounds, the temperature dependence of the pyroelectric current density and electric polarization were obtained for several x values and are displayed in Fig.1.6.3 [21]. It was seen that an increase in Fe^{3+} concentration leads to a decrease of both T_c and the polarization's magnitude, being attributed to the gradual fading out of the cycloidal spin ordering with increasing x, and thus, leading to a suppression of ferroelectricity for x ≥ 0.05.

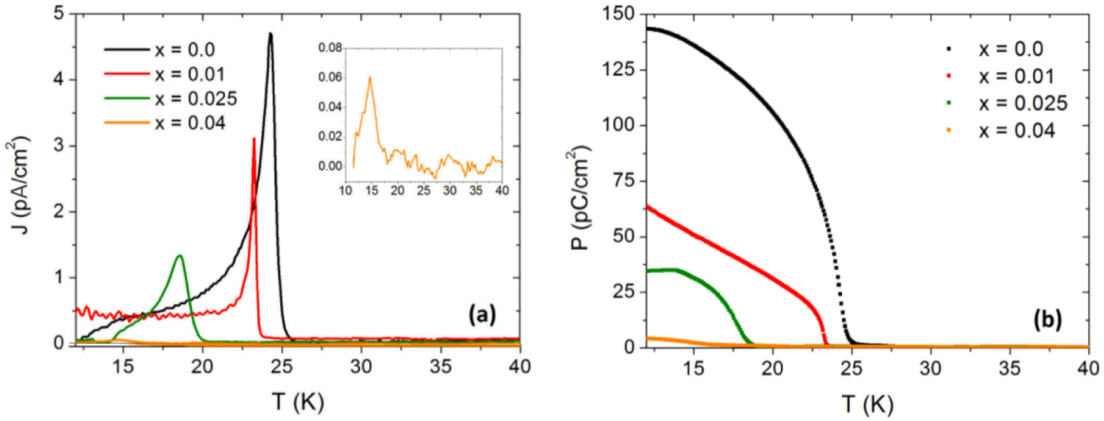

Figure 1.6.3: (a) Temperature dependence of the pyroelectric current density and (b) of the electric polarization for several x values. The inset in panel (a) shows the pyroelectric current for the sample with x $= 0.04$. Adapted from [21].

The magnetic field dependence of the relative electric polarization, $P(H)/P(H=0)$, at $T = 5$ K is shown in Fig.1.6.4 for several x values [21]. For $TbMnO_3$, practically no changes in the relative electric polarization were observed up to 4 T, in accordance with the results reported in [5]. Remarkably, the sensitivity of the relative electric polarization to an applied magnetic field drastically increases with increasing x. For x $= 0.04$, a 35% reduction of the relative polarization is achieved already at 1 T, increasing to more than 90% with an applied magnetic field above 4 T. Thus, the substitution of Mn^{3+} by Fe^{3+} appears to strengthen the magnetoelectric coupling, which is manifest in a strong magnetic field dependence of the electric polarization [21].

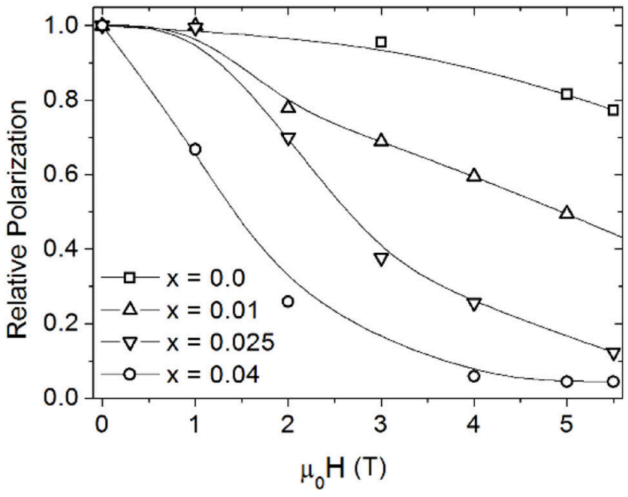

Figure 1.6.4: Relative electric polarization at $T = 5$ K as function of applied magnetic field for several x values in the $0 \leq$ x ≤ 0.04 concentration range. Adapted from [21].

It is worth stressing once more that all the aforementioned studies were performed in ceramics, concealing any anisotropic effects. As it was previously seen, the effect of

an applied magnetic field in both the magnetic structure and the electric polarization of $TbMnO_3$ largely depends on the direction along which such field is applied. Therefore, it is utterly relevant to study how the Fe^{3+} concentration influences those behaviors in the multiferroic region of the $TbMn_{1-x}Fe_xO_3$ system.

1.7 Purpose of this Dissertation

This dissertation aims at dwelling further into the work started by R. Vilarinho in understanding the physical mechanisms underlying the magnetoelectric properties of the multiferroic region of the $TbMn_{1-x}Fe_xO_3$ system. As the effect of an applied magnetic field in both the magnetic structure and the electric polarization of $TbMnO_3$ largely depends on the direction along which such field is applied, it is utterly relevant to study how the Fe^{3+} concentration influences those behaviors in the multiferroic region of the $TbMn_{1-x}Fe_xO_3$ system. Therefore, to understand in a more detailed way the physical properties of the multiferroic region of $TbMn_{1-x}Fe_xO_3$ and how the polarization and magnetic structure are coupled, a detailed study of the temperature and magnetic field dependence of the polar, dielectric and magnetic properties of oriented single crystals of $TbMn_{0.98}Fe_{0.02}O_3$ and $TbMn_{0.96}Fe_{0.04}O_3$ was performed. The obtained results also allow to complement neutron diffraction measurements under applied magnetic field, previously performed by R. Vilarinho in an oriented single crystal of $TbMn_{0.98}Fe_{0.02}O_3$ [15]. Furthermore, to grasp how such macroscopic behaviors emerge, one must turn its attention to the underlying microscopic mechanisms and how they evolve with x. Hence, the electromagnon spectra of $TbFe_{0.04}Mn_{0.96}O_3$ is obtained through THz time-domain spectroscopy and the spin-phonon coupling is investigated in the compounds with x $= 0, 0.02$ and 0.04 through Raman scattering experiments.

Chapter 2

Experimental Techniques

The vast majority of the experimental work involved in this thesis was split between the group of Polarizable Materials and Magnetoelectric Nanostructures at the Institute of Physics for Advanced Materials, Nanotechnology and Photonics (IFIMUP) in Porto, Portugal and the group of Infrared and Dielectric Spectroscopy at Institute of Physics of the Czech Academy of Sciences (FZU) in Prague, Czech Republic. All of the $TbMn_{1-x}Fe_xO_3$ single crystals with $x = 2, 4\,\%$ were provided by the group of Marian Mihalik from the Institute of Experimental Physics of the Slovak Academy of Sciences in Košice, Slovak Republic.

2.1 Sample Preparation

The samples of $TbFe_{0.02}Mn_{0.98}O_3$ were oriented and cut by the group group of Marian Mihalik. The samples of $TbFe_{0.04}Mn_{0.96}O_3$ that were characterized at IFIMUP were oriented using a X-ray diffractometer at the Department of Physics of the University of Coimbra and cut at IFIMUP using a diamond wire. This method is not the most suited and can lead to considerable misalignments. However, for polar and dielectric measurements, an error of $\sim 10^{\circ}$ is not critical. The samples were again oriented and then polished to be plane-parallel with optical quality using diamond paste at the optical workshop of FZU. In those samples, the orientation of the crystal axes is known with an error less than 1°. This was of utmost importance as THz time-domain spectroscopy measurements require plane-parallel samples with precisely oriented crystal axes. Those samples were also used for polar measurements with applied magnetic field at FZU. For polar and dielectric measurements, gold electrodes with the largest possible area were sputtered.

2.2 Complex Electric Permittivity

In the $1\,\text{Hz} - 1\,\text{MHz}$ frequency range, the complex electric permittivity can be obtained by directly measuring the capacitance and dielectric loss of a plane plate capacitor, where

the dielectric is the sample being studied. The experimental method is based on the electrical impedance analysis of an electric circuit that contains the capacitor formed by the sample. The frequency and temperature dependences of the real, ϵ', and imaginary, ϵ'', parts of the complex electric permittivity are calculated from the capacitance, C, and dielectric loss, $tan\delta$:

$$\epsilon' = \Big(\frac{d}{\epsilon_0 A}\Big)C, \quad \epsilon'' = \epsilon' tan\delta \tag{2.2.1}$$

where ϵ_0 is the vacuum permittivity, A is the electrode area and d is the thickness. The dielectric characterization at zero magnetic field was done at IFIMUP. The applied AC electric field had an amplitude of $1\,\mathrm{V/cm}$ and frequency ranging from $1\,$kHz to $1\,$MHz. An $HP4284A$ impedance analyzer was used, having a resolution better than $100\,$mHz in the considered frequency range. The measurements were carried out in cooling and heating runs in the $8 - 300\,$K temperature range, with a constant rate of $0.5\,\mathrm{K/min}$. The sample was placed in a closed-cycle He cryostat and its temperature was known with an accuracy of $0.1\,$K. The dielectric characterization with applied magnetic field was performed at FZU in a similar way but using a cryostat equipped with a $19.5\,$T superconducting coil. In this case, the frequency and temperature ranged from $1\,$Hz to $1\,$MHz and from $1\,$K to $50\,$K, respectively.

2.3 Pyroelectric Current

Typically, the spontaneous polarization cannot be detected by measuring surface charges because the depolarizing field, which arises from such charge distribution, is compensated by the flux of free charges in both the crystal and the electrodes. However, if the polarization is a function of temperature, it can be obtained by measuring the pyroelectric current. The polar characterization of the samples then consists in calculating the change in electric polarization as a function of temperature by integrating in time the measured pyroelectric current density. To promote an electric dipole alignment between different domains, the samples are cooled from the paraelectric phase with an applied electric field, the so-called poling field. The pyroelectric current is then measured, with the poling field turned off and after short-circuiting the sample's terminals to promote the release of spurious charges, while heating with a constant temperature rate. The pyroelectric current is obtained by measuring the voltage drop on a calibrated resistance in parallel with the sample (Fig.2.3.1). The value of that resistance should be 10 to 100 times lower than that of the sample and as high as possible in order to increase the resolution, for which a $10^{10}\,\Omega$ resistance was used.

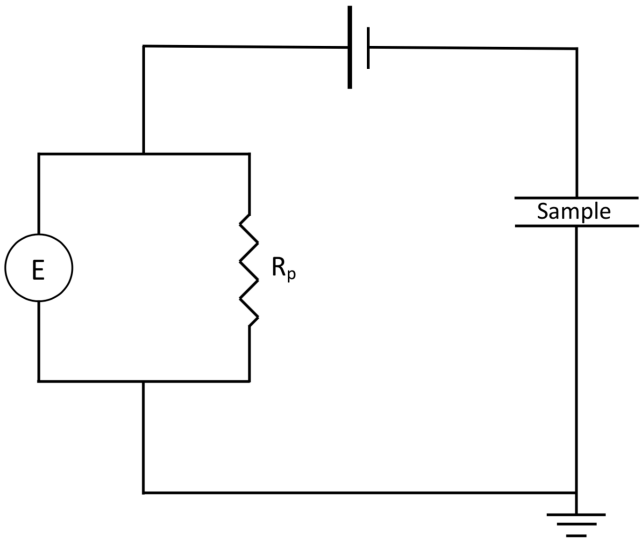

Figure 2.3.1: Electric circuit used for pyroelectric current measurements. The electrometer and the calibrated resistance are represented by E and R_p, respectively.

The first polar characterization of the samples was carried out at IFIMUP. The electrometer used was a Keithley 617 with a resolution of 0.5 pA. The measurements were carried out in the $10 - 300$ K temperature range and the sample's temperature was known with an accuracy of at least 0.1 K. Because it was a first characterization, measurements with several poling fields ($4 - 100$ V/mm) and temperature rates between 2 K/min and 10 K/min were performed. This was done because there can be charges in the electrodes that originate from something other than the polarization of the sample.

To study the polarization's dependence on an applied magnetic field, pyroelectric current measurements were also performed in a similar way at FZU in standard Quantum Design Physical Properties Measurement System (PPMS) equipped with 9 T and 14 T superconducting coils. All measurements were performed in the $2 - 50$ K temperature range with a 5 K/min heating rate. A poling field of 100 V/mm was always applied at 50 K. The magnetic field was applied in the paramagnetic phase and, unlike the poling electric field, it remained on during the measurements.

2.4 Magnetic Properties

The magnetic properties of $TbMn_{0.96}Fe_{0.04}O_3$ were studied using a SQUID (Superconducting Quantum Interference Devices) magnetometer by Quantum Design at IFIMUP. The resolution in the magnetization measurements is better than 5×10^{-7} emu. The measurements were performed in the $5 - 300$ K temperature range, where the temperature was controlled through a liquid helium flux. Detailed information concerning the SQUID magnetometer can be found in [62]. The low field temperature dependence of the magnetization was measured in heating runs. The measurements were made both in zero field cooling (ZFC) and field cooling conditions (FC), with an applied magnetic field of

40 Oe. Also, isothermal magnetic hysteresis loops measurements were obtained at 5 K as a function of the applied magnetic field, which varied from -5.5 to 5.5 T. The measurements performed to study the magnetic properties of $TbMn_{0.98}Fe_{0.02}O_3$ are very similar to what was previously described and were made by the group of M. Mihalik at the Institute of Experimental Physics of the Slovak Academy of Sciences.

2.5 THz time-domain Spectroscopy

The THz time-domain measurements were performed at FZU. The thickness of the samples used in these experiments are in the $0.5 - 1$ mm range. A scheme of the homemade spectrometer is shown in Fig.2.5.1 (a more thorough description can be found in [63]).

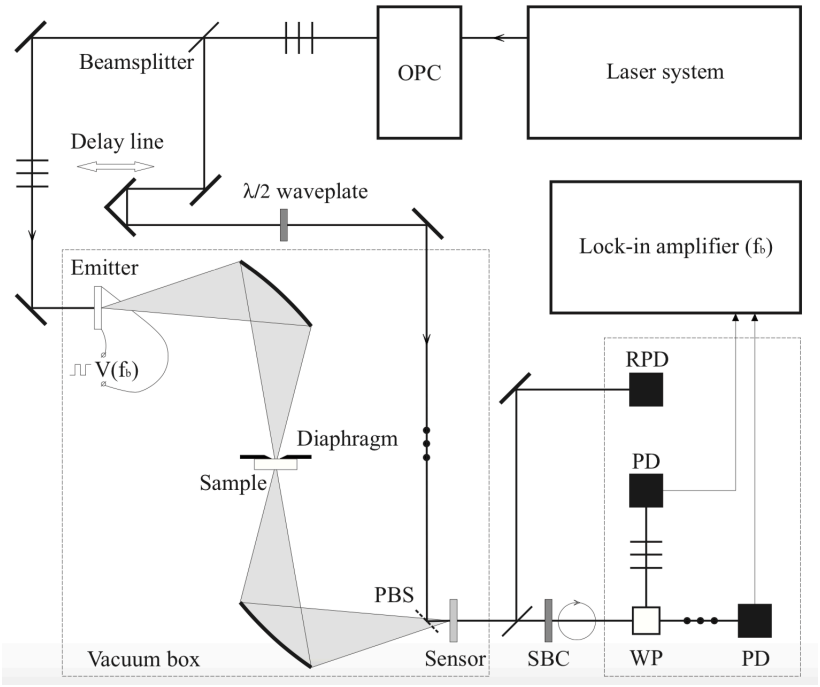

Figure 2.5.1: Schematic layout of the THz time-domain spectrometer at FZU. Taken from [63].

The horizontally polarized beam of femtosecond laser pulses produced by the laser system (Mira Seed, 67 fs long pulses, 76 MHz repetition rate, 8 nJ per pulse, 800 nm, 650 mW average output) is split into pump and sampling beams with intensities corresponding to 96 % and 4 % of the initial beam, respectively. The pump beam goes to an emitter, generating THz radiation. An ellipsoidal mirror focuses the generated THz radiation on the sample, which is fixed in a way that covers the whole aperture of the diaphragm. The transmitted THz radiation is then focused on the electro-optic sensor ($ZnTe$ crystal) by another mirror.

At the same time, the sampling beam passes through an optical delay line and a half-wave plate. After its reflection on a pellicle beam-splitter (PBS), which is fully transparent

for THz radiation, it propagates colinearly with the THz beam through the sensor crystal. The sampling beam is then split into two beams. One of them goes to a reference photodiode (RPD), and the second one propagates through a Soleil-Babinet compensator (SBC), acting as an adjustable quarter-wave plate. The circularly polarized sampling beam is spatially separated into horizontally and vertically polarized beams by a Wollaston prism (WP) and the difference between their intensities is measured by two balanced photodiodes. The difference signal, which is proportional to the THz field, is transferred to a lock-in amplifier synchronized with the frequency of a step-like bias field applied to the emitter. The lock-in amplifier's output is normalized by the signal from the reference photodiode.

The region where the THz pulses propagate is enclosed in a vacuum box to avoid interaction of the THz radiation with water vapor. The spectrometer is equipped with a liquid He cooled continuous flow cryostat with thin mylar windows, which are well transparent for THz radiation.

The spectroscopic method in the transmission geometry involves the measurement of a reference wave form, $E_{ref}(t)$, with an empty sample holder or with a known reference sample, as well as the signal wave form, $E_{sign}(t)$, corresponding to the sample being studied. If scattering on inhomogeneities of the sample, surface irregularities and diffraction on aperture edges can be neglected, the complex transmission coefficient is simply given by [63, 64]:

$$t(f) = \frac{E_{sign}(f)}{E_{ref}(f)} \tag{2.5.1}$$

Considering a homogeneous sample in the form of a plane-parallel dielectric slab [63, 64],

$$t(f) = \sum_{j=0}^{m} t_j(f) = \frac{4Ne^{2\pi if(N-1)d/c}}{(N+1)^2} \sum_{j=0}^{m} \left(\frac{N-1}{N+1} e^{2\pi ifNd/c} \right)^{2j} \tag{2.5.2}$$

where d is the sample's thickness, c is the speed of light in vacuum, m is the number of internal double reflections (echoes) in the sample and $t_j(f)$ are the individual contributions of the internal reflections ($j \neq 0$) or of a direct pass ($j = 0$). The previous equation can be numerically solved for the complex index of refraction, $N(f) = n(f) + ik(f)$ [65]. Because in THz time-domain spectroscopy the time profile of the electric field is measured and not just its power, the amplitude and phase of each frequency component of the THz pulse are known. Thus, the real and imaginary parts of N can be calculated at every frequency within the usable bandwidth of the THz pulse, with no need to employ the Kramers-Kronig relations.

2.6 Raman Scattering

The Raman scattering experiments were performed at IFIMUP, using a Raman inVia Qontor Renishaw spectrometer. The spectrometer is based in lenses directly coupled to a

vertical microscope, equipped with a high sensitivity CCD detector with 1024×256 pixels and cooled to -70 ºC by Peltier effect. The equipment has filters for 532, 633 and 785 nm laser excitations. The chosen laser line for all measurements was the 532 nm one, for which Stokes and anti-Stokes measurements in the $10 - 4000$ cm^{-1} range are possible. High efficiency diffraction gratings are available with 1200, 1800 and 2400 lines/mm. The 2400 lines/mm one was used in all experiments, allowing for a high spectral resolution (better than 2 cm^{-1} in the whole spectral range). The unpolarized Raman spectra as a function of temperature were obtained by placing the sample in a closed-cycle helium cryostat, with a $10 - 300$ K temperature range. The laser power was carefully chosen in order to avoid heating the sample (3.3 mW, corresponding to 10 % of the laser power).

The obtained Raman spectra were analyzed using both the commercial *Igor Pro* software and an automated Python based algorithm, developed by Catarina Dias and Rui Vilarinho. In both cases, the Raman spectra are simulated through a sum of damped oscillators [66]:

$$I(\omega, T) = [1 + n(\omega, T)] \sum_{j=1}^{N} A_{oj} \frac{\omega \Omega_{oj}^2 \Gamma_{oj}}{(\Omega_{oj}^2 - \omega^2)^2 + \omega^2 \Gamma_{oj}} \tag{2.6.1}$$

where $n(\omega, T)$ is the Bose-Einstein factor and A_{oj}, Ω_{oj}, Γ_{oj} are the strength, wavenumber and damping coefficient of the jth oscillator, respectively.

Chapter 3

Magnetoelectric Effect in $TbMn_{1-x}Fe_xO_3$ with $x = 0.02, 0.04$

All the previous studies in the multiferroic region of the $TbMn_{1-x}Fe_xO_3$ solid solution relied on polycrystalline samples [20, 21, 22]. Thus, any anisotropic features exhibited by the electric polarization and magnetic properties were completely smeared out. Because such features play important roles in the pure compound, they are assumed to be particularly important in the multiferroic region of the solid solution ($x < 0.05$) as well. In particular, the direction of the applied magnetic field has interesting effects on the magnetic structure, some of which inferred by the switching of the polarization's direction from the c to the a axis, according to Eq.1.4.7 [5]. To understand in a more detailed way the physical properties of the multiferroic region of $TbMn_{1-x}Fe_xO_3$ and how the polarization and magnetic structure are coupled, a detailed study of the temperature and magnetic field dependence of the polar, dielectric and magnetic properties of oriented single crystals of $TbMn_{0.98}Fe_{0.02}O_3$ and $TbMn_{0.96}Fe_{0.04}O_3$ is presented in this chapter. Neutron diffraction results in $TbMn_{0.98}Fe_{0.02}O_3$ are also discussed in connection with the polar measurements, allowing a much deeper understanding of the underlying microscopic effects.

3.1 Magnetic and Dielectric Properties

The temperature dependence of the magnetization measured in zero-field cooling (ZFC) and field-cooling (FC) conditions and magnetic isotherms of $TbMn_{0.98}Fe_{0.02}O_3$ (at 2 K) and of $TbMn_{0.96}Fe_{0.04}O_3$ (at 5 K), measured along each crystallographic axis, is shown in Fig.3.1.1.

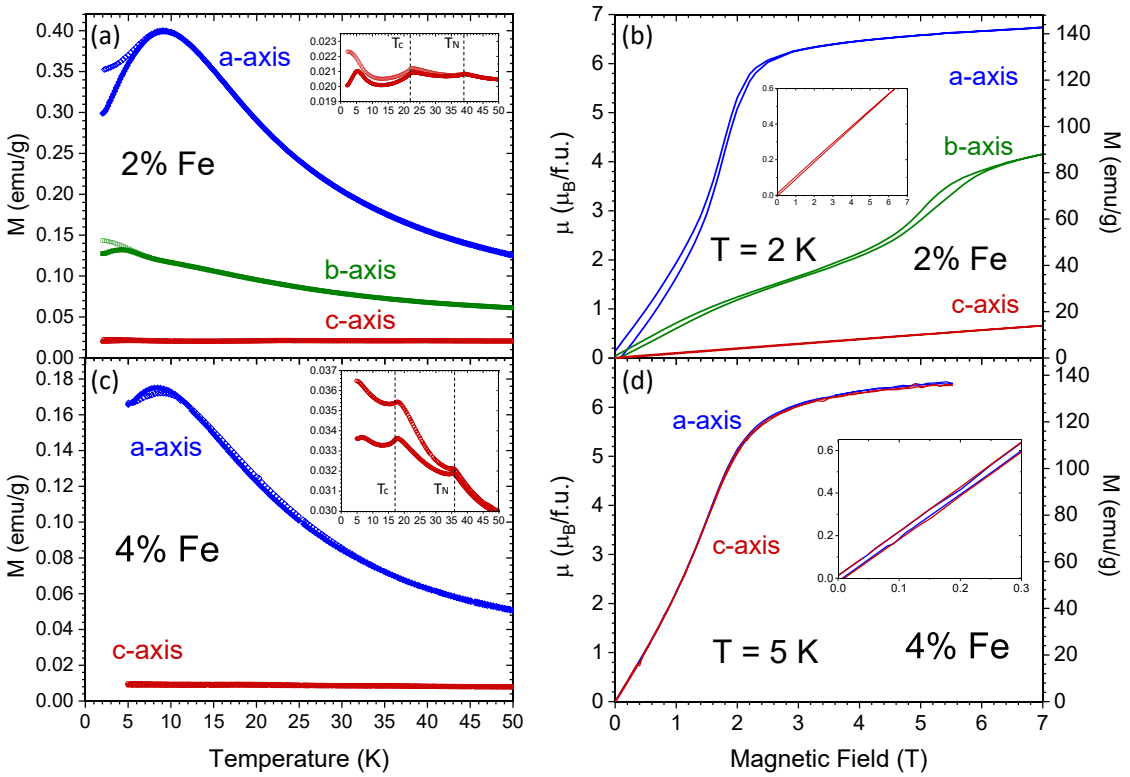

Figure 3.1.1: (a) Magnetization and (b) magnetic isotherms at $T = 2$ K of $TbMn_{0.98}Fe_{0.02}O_3$, measured along each crystallographic axes by the group of M. Mihalik. (c) Magnetization and (d) magnetic isotherms at $T = 5$ K of $TbMn_{0.96}Fe_{0.04}O_3$ measured along the a and c axes. In panels (a) and (c), the filled and empty points represent magnetization measurements in zero field cooling (ZFC) and field cooling (FC) conditions, respectively.

It is clear that, for both compounds, the magnetization measured along the a axis is considerably larger than the one along the c axis. This is consistent with the c axis being the hard magnetization axis, as previously reported for $TbMnO_3$ [5]. For $TbMn_{0.98}Fe_{0.02}O_3$ ($TbMn_{0.96}Fe_{0.04}O_3$), the anomalies associated with the stabilization of the sinusoidal collinear order of the Mn^{3+} spins at $T_N \approx 38$ K ($T_N \approx 36$ K), the spin cycloid ordering below $T_c \approx 28$ K ($T_c \approx 17$ K) and the ordering of the Tb^{3+} ions below $T_N^{Tb} \approx 6$ K are only seen in the magnetization curve along the c axis. These temperatures are in good agreement with the ones previously reported in ceramics [21]. It is clear that both T_c and T_N decrease with increasing x, showing that the presence of Fe^{3+} destabilizes the sinusoidal and cycloidal phases. Below 40 K, for both compounds, the magnetization curves measured in

ZFC display smaller values than the ones measured in FC conditions. Therefore, the field applied while cooling induces a magnetization in the system, suggesting a weak ferromagnetic (WFM) character of the magnetic phases below that temperature. It is interesting to notice that the splitting in the magnetization curve along the c axis is considerably larger in the x $= 0.04$ compound than in the compound with x $= 0.02$. Furthermore, only a small splitting along the c axis is observed in $TbMnO_3$ (see Fig.1.2.2 (a)). The strong anisotropy in these compounds is also evidenced by the different behavior of the magnetic isotherms along each crystallographic axis. In $TbMn_{0.98}Fe_{0.02}O_3$, the magnetic isotherm measured at 2 K along the a axis resembles the one of a ferromagnet. The opening of the magnetic isotherm along the b axis at low fields and also at roughly 5.5 T hints for an AFM character, while the straight line shape along the c axis resembles the behavior of a paramagnet. On the other hand, the behavior of the magnetic isotherms in $TbMn_{0.96}Fe_{0.04}O_3$ is quite different. While the magnetic isotherm along the a axis is similar to the other compound, it is striking to observe such behavior of the magnetic isotherm along the c axis. This is rather surprising as, apart from a larger splitting in the magnetization curves measured along the c axis, the temperature dependence of the magnetization is quite similar between the two compounds. This suggests that the magnetic structure of $TbMn_{0.96}Fe_{0.04}O_3$ displays an intricate behavior, which may be associated with the fact that x $= 0.04$ is near the border of the multiferroic region of the $TbMn_{1-x}Fe_xO_3$ system. Unfortunately, it was not possible to measure neither the temperature dependence of the magnetization nor the magnetic isotherm along the b axis. As it was also not possible to perform magnetization measurements in $TbMn_{0.98}Fe_{0.02}O_3$ at higher temperatures in oriented single crystals, the temperature dependence of the magnetization up to 300 K of a non-oriented crystal of that compound is shown in Fig. 3.1.2, along with the temperature dependence of the magnetization along the c axis of $TbMn_{0.96}Fe_{0.04}O_3$. Similarly to $TbMnO_3$ (see Fig.1.2.2 (b)), a broad peak is observed around 120 K. The position and shape of this peak do not appear to be largely affected by the presence of Fe^{3+} and its origin remains an open question. However, in the following chapters, it will be seen that this broad anomaly appears to be associated with the emergence of magnetic interactions at temperatures considerably higher than T_N.

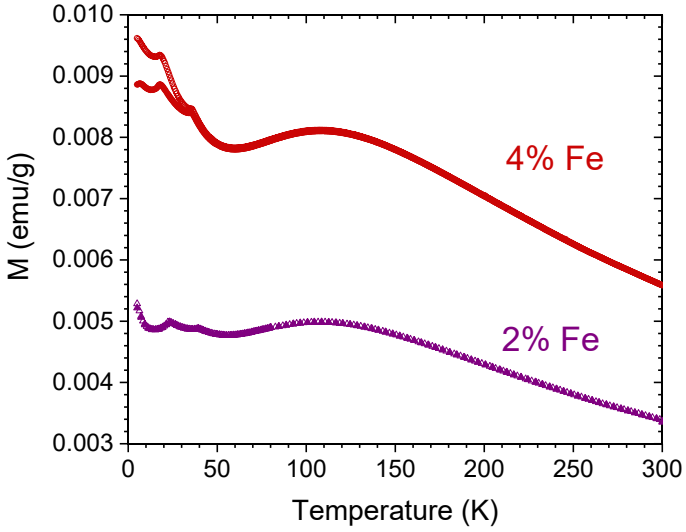

Figure 3.1.2: Temperature dependence of the magnetization along the c axis of $TbMn_{0.96}Fe_{0.04}O_3$ and of a non-oriented crystal of $TbMn_{0.98}Fe_{0.02}O_3$. The filled and empty points represent measurements with zero field cooling (ZFC) and field cooling (FC), respectively. The measurement in $TbMn_{0.98}Fe_{0.02}O_3$ was performed by R. Vilarinho.

The temperature dependence of the real, ϵ', and imaginary, ϵ'', parts of the electric permittivity of $TbMn_{0.98}Fe_{0.02}O_3$ and $TbMn_{0.96}Fe_{0.04}O_3$ measured along the a and c axes at several frequencies are displayed in Fig.3.1.3 and Fig.3.1.4, respectively. In both compounds, two different kinds of anomalies can be ascertained in the imaginary part of the electric permittivity. The first, also present in the real part of the electric permittivity, is characterized by a frequency independent maximum at T_c and marks the transition from the sinusoidal to the cycloidal phase. On the other hand, the second kind displays a frequency dependent maximum that shifts to higher temperatures with increasing frequency and is a consequence of dielectric relaxation processes. The $\epsilon_a^{'}(T)$, $\epsilon_c^{'}(T)$ and $\epsilon_a^{''}(T)$ curves exhibit a change of slope at T_N, marking the phase transition from the paramagnetic to the sinusoidal phase in the two compounds. However, this is not observed in the $\epsilon_c^{''}(T)$ curve due to the presence of dielectric relaxations near T_N. Furthermore, no anomalies can be found around 120 K that could shed some light in the origin of the observed broad anomaly in the temperature dependence of the magnetization (see Fig.3.1.2).

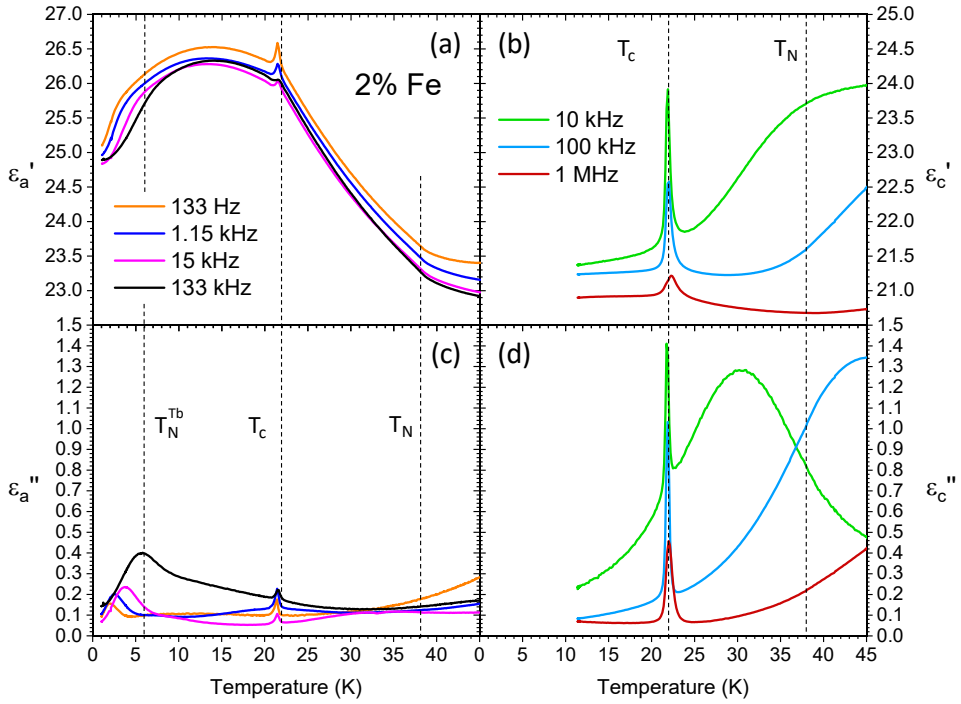

Figure 3.1.3: Temperature dependence of the real, ϵ', and imaginary, ϵ'', parts of the electric permittivity of $TbMn_{0.98}Fe_{0.02}O_3$, measured along the a and c axes at several frequencies.

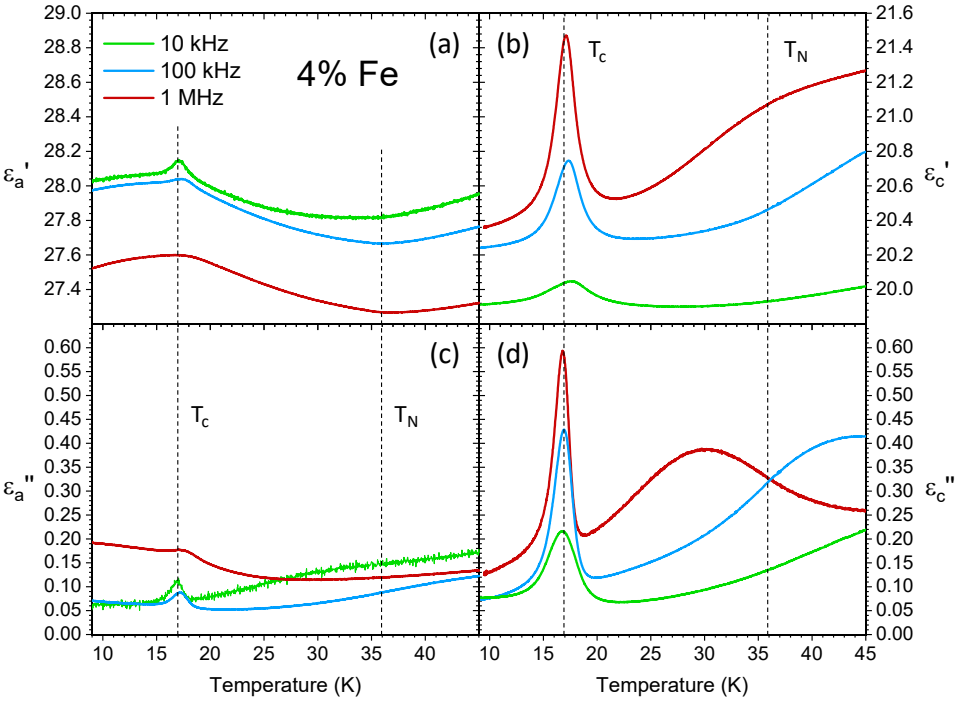

Figure 3.1.4: Temperature dependence of the real, ϵ', and imaginary, ϵ'', parts of the electric permittivity of $TbMn_{0.96}Fe_{0.04}O_3$, measured along the a and c axes at several frequencies.

To take a step further towards unravelling the magnetic structure of these compounds, neutron diffraction was performed by R. Vilarinho in an oriented single crystal of $TbMn_{0.98}Fe_{0.02}O_3$ [15]. The transition from the paramagnetic to the incommensurate sinusoidal phase is revealed by the appearance of a satellite peak indexed to $(0, q_m, 1)$, with $q_m = 0.28$ at $T_N = 38$ K [15]. To discuss the commensurability of the spin cycloidal phase and whether or not it affects ferroelectricity, the temperature dependence of q_m is depicted in Fig.3.1.5 (a).

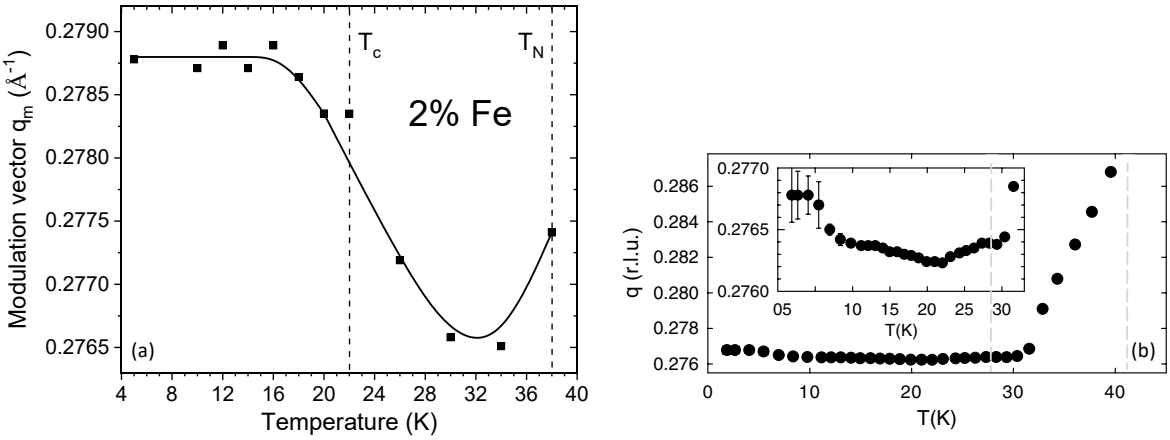

Figure 3.1.5: Temperature dependence of the b component of the modulation vector, $(0,\ q_m,\ 1)$ for (a) $TbMn_{0.98}Fe_{0.02}O_3$ and (b) $TbMnO_3$. Dashed vertical lines mark T_c and T_N, while the solid line is a guide for the eye. Adapted from [30, 15].

While the values of q_m are very similar to those reported in $TbMnO_3$, its temperature dependence is quite distinctive [29, 30]. First of all, in the sinusoidal phase, q_m decreases below $T_N = 38$ K, reaches a minimum value at ~ 32 K and then increases down to T_c. On the other hand, in $TbMnO_3$, q_m steeply decreases from T_N to T_c [29, 30]. Regarding the spin cycloidal phase, it seems that, within experimental error, q_m reaches a constant value below $\sim$ 17K. Interestingly, the modulation vector seems closer to be locked in than in $TbMnO_3$, even though it only happens well below T_c. Therefore, the presence of Fe^{3+} seems to have a considerable influence on the behavior of the modulation vector in both the magnetically ordered phases. Once again, in these compounds, the commensurability of the cycloidal phase seems to have no influence in ferroelectricity whatsoever [30].

3.2 Magnetoelectric Properties of $TbMn_{0.98}Fe_{0.02}O_3$

Figure 3.2.1 shows the temperature dependence of ϵ_a' and ϵ_a'', measured at 133 Hz under several magnetic fields applied along the b axis. For a magnetic field strength of 5.5 T, the amplitude of the anomaly at T_c is even smaller than at zero applied field and a broad peak appears in ϵ_a' at $\sim$ 5 K, while at 8 T, it is barely noticeable and a large peak appears in ϵ_a' at $\sim$ 12 K. The position of the peak at T_c is independent of the applied magnetic field, at least up to 8 T. The appearance of such low temperature anomalies in ϵ_a above 5 T points towards a transition to a ferroelectric phase with polarization along the a axis instead [5]. Below 10 K, ϵ_a'' exhibits a frequency dependent peak at 0 T, a double peak at 5.5 T and no such peaks are discernible at 8 T. Because the temperatures at which these peaks appear are below T_N^{Tb}, their origin probably lies in phenomena induced by the ordering of the Tb^{3+} ions.

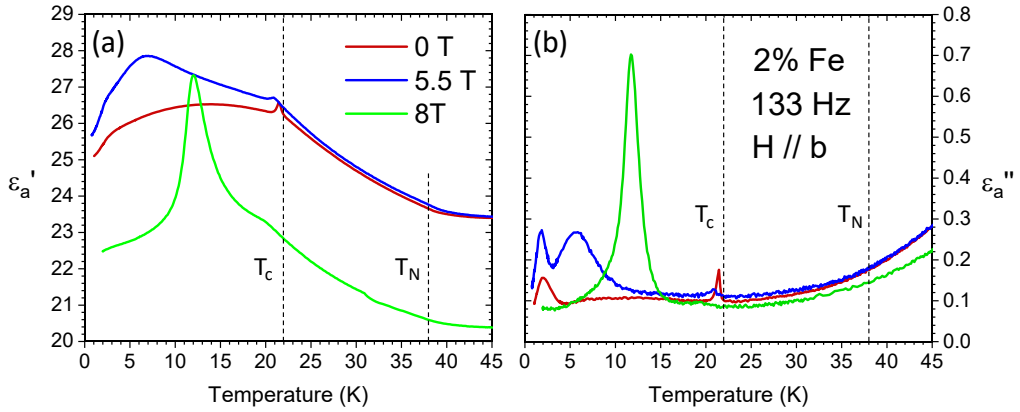

Figure 3.2.1: Temperature dependence of ϵ_a' and ϵ_a'', measured at a fixed frequency of 133 Hz and magnetic fields of 0, 5 and 8 T applied along the b axis, for $TbMn_{0.98}Fe_{0.02}O_3$. The dashed lines mark T_c and T_N at 0 T.

To unravel the effect of a magnetic field on the electric polarization, the pyroelectric current density, $J(T)$, was measured along the a and c axes under an applied magnetic field applied along the b axis. The results are shown in Fig.3.2.2.

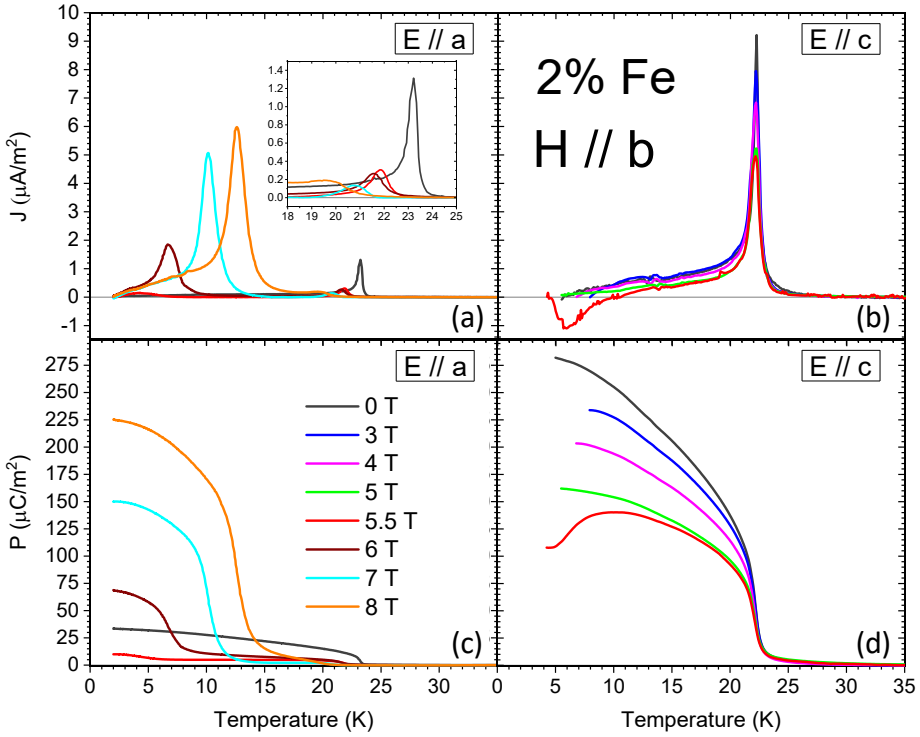

Figure 3.2.2: Temperature dependence of the pyroelectric current densities ((a), (b)) and electric polarization ((c), (d)) of $TbMn_{0.98}Fe_{0.02}O_3$, measured along the a and c axis under an applied magnetic field along the b axis.

At 0 T, a sharp anomaly in $J(T)$ measured along the c axis appears at $T_c = 22$ K, in agreement with the results from the magnetic and dielectric measurements. At least up to 8 T, such anomaly is independent of the applied magnetic field. Up to 5 T, the polarization along the c axis, P_c, decreases with increasing field strength. Concerning the results obtained along the a axis, apart from a projection of P_c due to small misalignment of the samples, nothing is detected along this axis. At 5 K, an applied field of 4 T reduces P_c to roughly $75\,\%$ of its value at 0 T. This behavior is quite different from the one reported in $TbMnO_3$, where practically no changes in P_c were found up to 4 T [5].

For a 5.5 T magnetic field strength, a negative peak in $J(T)$ along the c axis is observed below $\sim$ 6 K, concomitantly with a positive one in $J(T)$ measured along the a axis. Above 5.5 T, the anomaly in $J(T)$ measured along the a axis shifts to higher temperatures and increases in magnitude. This translates into a decrease in the electric polarization along the c axis for temperatures below the temperature at which the peak appears and, simultaneously, a polarization increase along the a axis. Thus, as hinted by electric permittivity measurements, a polarization flop from the c to a axis occurs for applied magnetic fields along the b axis larger than 5 T. In light of Eq.1.4.7 and following the same train of thought as Kimura et al. for $TbMnO_3$, one can attribute this polarization switching to the rotation of the cycloidal plane from the bc to the ab plane.

3.2.1 Effect of a Magnetic Field on the Magnetic Structure

To study how an applied magnetic field can affect the commensurability and stability of the spin ordered phases and its eventual connection with ferroelectricity, neutron diffraction with magnetic field applied along the b axis was performed by R. Vilarinho [15]. The temperature dependence of the b component of the modulation vector, $(0,\, q_m,\, 1)$, for several applied magnetic fields along the b axis, is depicted in Fig.3.2.3.

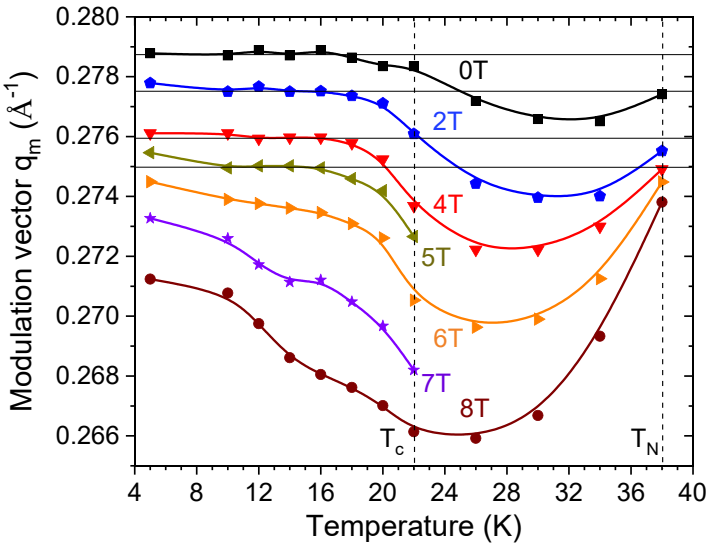

Figure 3.2.3: Temperature dependence of the b component of the modulation vector, $(0,\, q_m,\, 1)$, for several applied magnetic fields along the b axis. The dashed vertical lines mark T_c and T_N at 0 T. Adapted from [15].

It is striking how the applied magnetic field along the b axis changes the temperature dependence of the modulation vector. At fixed temperatures, its value decreases with increasing magnetic field. More importantly, above 5 T, q_m is never constant in the considered temperature range. Thus, an applied magnetic field along the b axis greatly disrupts the commensurability region that existed at 0 T. It is also interesting to see how the magnetic field affects the intensity of the peak assigned to the modulation of the cycloidal order, appearing below $T_c = 22$ K. The temperature dependence of the intensity of such peak, measured under several applied magnetic fields along the b axis, is shown in Fig.3.2.4 (a).

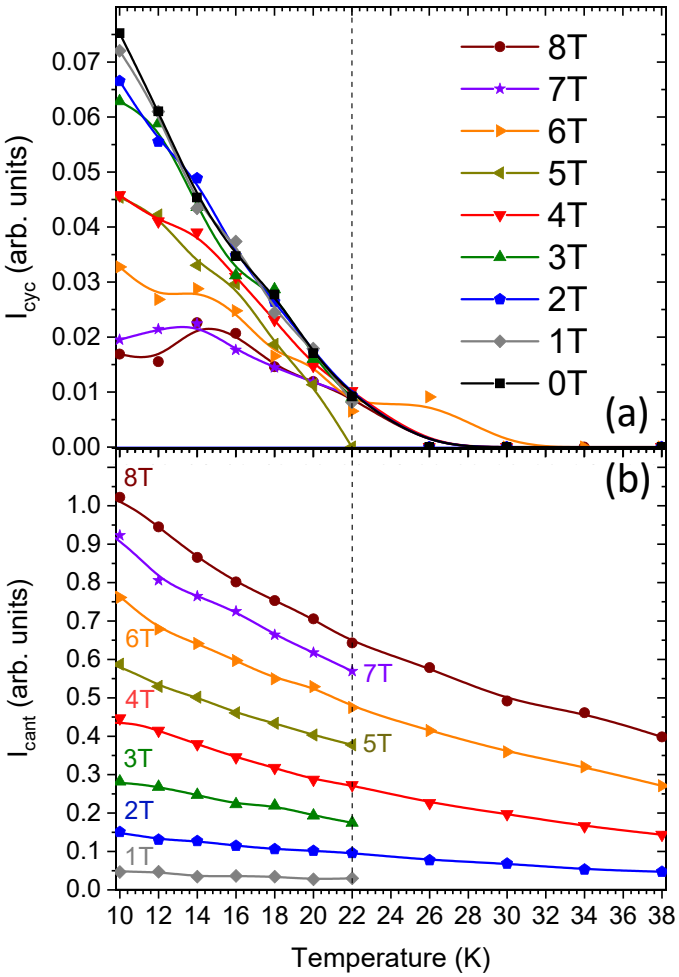

Figure 3.2.4: Temperature dependence of the intensity of magnetic diffraction peaks associated with the (b) cycloidal, I_{cyc}, and (c) canted, I_{cant}, spin structures for several applied magnetic fields along the b axis. Dashed vertical line marks T_c at 0 T. Adapted from [15].

For a fixed magnetic field strength, the intensity of the diffraction peak associated with the spin cycloidal structure increases with decreasing temperature from $T_c = 22$ K. However, for a fixed temperature, its intensity decreases with increasing magnetic field. At 10 K, the intensity reduces to ~ 75 % at 8 T, relatively to its value at 0 T. It seems that the applied magnetic field destabilizes the cycloidal spin structure. Remarkably, it also greatly enhances a diffraction peak assigned to a WFM component roughly along the a axis, corresponding to a spin-canted structure (Fig.3.2.4 (b)). Even though this peak is absent at 0 T, it is clearly present for an applied magnetic field strength of 1 T and appears already in the sinusoidal phase. For a given magnetic field/temperature, the intensity of the FM peak increases as the temperature decreases/magnetic field increases. To the best of the author's knowledge, there are not any neutron diffraction experiments in $TbMnO_3$, performed in similar conditions, with which to compare these results.

The aforementioned behaviors show that an applied magnetic field along the b axis greatly affects the temperature dependence of q_m in both the sinusoidal and cycloidal

phases. Also, the behavior of the FM peak indicates the presence of a spin-canting roughly along the a axis that is further enhanced by the applied magnetic field, being most likely accountable for the observed polarization decrease with increasing magnetic field. Furthermore, a magnetic field induced phase transition was observed for an applied magnetic field strength of approximately 6 T [15]. This is consistent with the results from the polar measurements, and thus, that phase transition is assigned to the rotation of the cycloidal plane from the bc to the ab plane.

3.3 Magnetoelectric Properties of $TbMn_{0.96}Fe_{0.04}O_3$

To gain further insight into the polar phase of this compound and how it is affected by an applied magnetic field, the pyroelectric current density was measured along the a and c axes under an applied magnetic field along each crystallographic axis. With magnetic field applied along the a and b axes, it was not possible to measure $J(T)$ along the a axis. This was due to technical difficulties arising from the samples jumping off the sample holder at moderately high magnetic fields. As the number of available single crystals is limited and the time it takes to properly orient and cut them is quite large, some relevant measurements are missing from this chapter and are left as future work. The temperature dependences of the pyroelectric current density and electric polarization measured along the c axis, with magnetic field applied along the a and b axes, are shown in Fig.3.3.1. It should be mentioned that, when the magnetic field is applied along the a axis, P_c at 0 T is much smaller than in all the other cases. This is simply due to the poling field being five times less than in all the other cases, due to experimental restrictions.

At 0 T, a sharp anomaly in the pyroelectric current density along the c axis appears at $T_c = 17$ K, in accordance with the results from the magnetic and dielectric measurements. Both T_c and the magnitude of the polarization at 0 T are further reduced relatively to the compound with x $= 0.02$, which is expected as an increase in x should further disrupt the spin cycloidal ordering. When the magnetic field is applied along the b axis, a small negative magnetic field dependent current peak appears below 7 K in the $1 - 3$ T range. A similar behavior is observed in $TbMnO_3$ (see Fig.1.2.3) and is ascribed to effects arising from the ordering of the Tb^{3+} ions [5]. Similarly to $TbMn_{0.98}Fe_{0.02}O_3$ but unlike $TbMnO_3$, P_c decreases with increasing magnetic field. Surprisingly, P_c is practically suppressed with a magnetic field of 8 T applied along the b axis, while it is suppressed already at 5.5 T when the applied field is along the a axis. This is quite different from what is reported in $TbMnO_3$, where the polarization switches direction for a large enough applied magnetic field along either those axes (see Fig.1.2.5) [5].

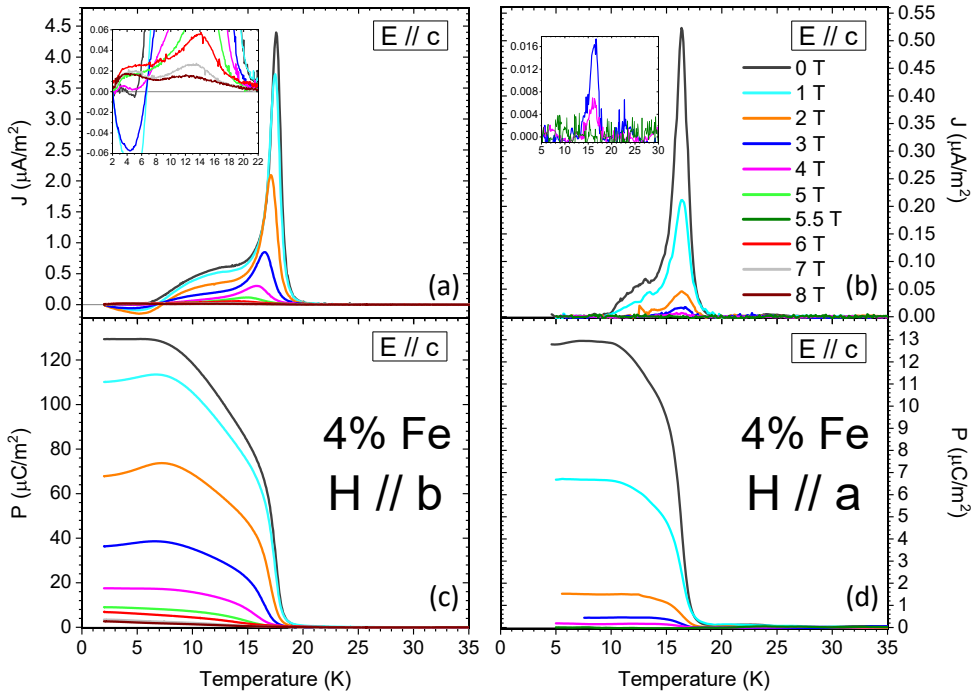

Figure 3.3.1: Temperature dependence of the ((a), (b)) pyroelectric current density and ((c), (d)) electric polarization of $TbMn_{0.96}Fe_{0.04}O_3$, measured along the c axis under an applied magnetic field along the a and b axes. When the magnetic field is applied along the a axis, the poling field is five times less than when applied along the b axis.

As previously mentioned, a magnetic field above 7 T along the c axis suppresses the ferroelectricity below a certain temperature in $TbMnO_3$ [5]. That temperature increases with increasing magnetic field and, above 13 T, the ferroelectricity is completely suppressed [5]. However, what happens in $TbMn_{0.96}Fe_{0.04}O_3$ is quite different as, before the ferroelectricity being completely suppressed, a non-zero polarization is always present at all temperatures below T_c. Thus, these results clearly point towards a magnetic field induced suppression of the ferroelectricity, although pyroelectric current measurements along the a axis should be performed to confirm this beyond doubt. It was seen that, for $x = 0.02$, a magnetic field applied along the b axis promotes a spin-canting roughly along the a axis. Thus, it is reasonable that an increase in x should enhance such spin-canting, further disrupting the cycloidal spin order and eventually leading to the suppression of ferroelectricity. However, in $TbMn_{0.96}Fe_{0.04}O_3$, such suppression is also observed when the magnetic field is applied along the a axis, happening at an even lower field strength. Therefore, spin-canting appears to be even more enhanced by an applied magnetic field along the a axis.

The temperature dependence of the pyroelectric current density measured along both the a and c axes under an applied magnetic field along the c axis was also measured and the results are depicted in Fig. 3.3.2. Remarkably, this also yielded some rather interesting results.

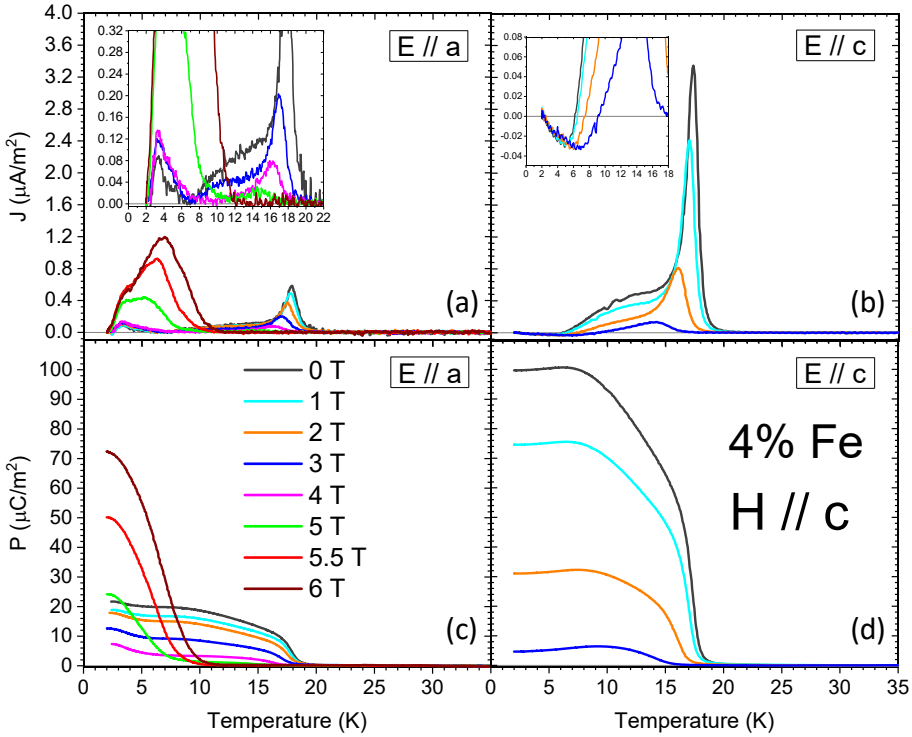

Figure 3.3.2: Temperature dependence of the ((a), (b)) pyroelectric current densities and ((c), (d)) electric polarization of $TbMn_{0.96}Fe_{0.04}O_3$, measured along the a and c axes under an applied magnetic fields along the c axis.

Both P_a and P_c decrease with increasing magnetic field up to 4 T. Opposite peaks are observed in $J(T)$ below 8 K for magnetic field strengths in the $0 - 3$ T range. Below 3 T, such peaks are independent of the applied magnetic field. However, above 3 T, a broad positive peak emerges at low temperatures in $J(T)$ measured along the a axis and, for higher fields, it shifts to higher temperatures and its amplitude increases. This translates into an increase in polarization along the a axis for temperatures below the temperature at which the peak appears. As the current along the c axis could not be measured above 3 T, it is not possible to claim with complete certainty that this is indeed a polarization flop, although there are strong indications of such.

In this case, the matter of obtaining a non-zero polarization along the a axis at 0 T deserves further discussion. As previously described, the samples with $x = 0.04$ were polished with optical quality and there is an error of less than 1^o in the orientation of the crystal axes. Therefore, it seems unlikely that the non-zero P_a at 0 T can be ascribed to misalignments, like in the samples with $x = 0.02$. It is then reasonable to think that the cycloidal plane can actually be rotated from the bc plane. As the cycloidal propagation vector should remain along the b axis, such rotation must occur along that same axis[1].

[1] A similar magnetic field induced rotation of the cycloidal plane was recently reported in $Gd_{0.5}Dy_{0.5}MnO_3$ [58].

Furthermore, the angle between the cycloidal and bc planes, θ, can be estimated by:

$$tan\theta = \frac{P_a}{P_c}, \tag{3.3.1}$$

where P_a and P_c are considered at the same fixed temperature. Considering P_a and P_c at the lowest measured temperature, it is depicted in Fig.3.3.3 how θ evolves with applied magnetic field along the c axis.

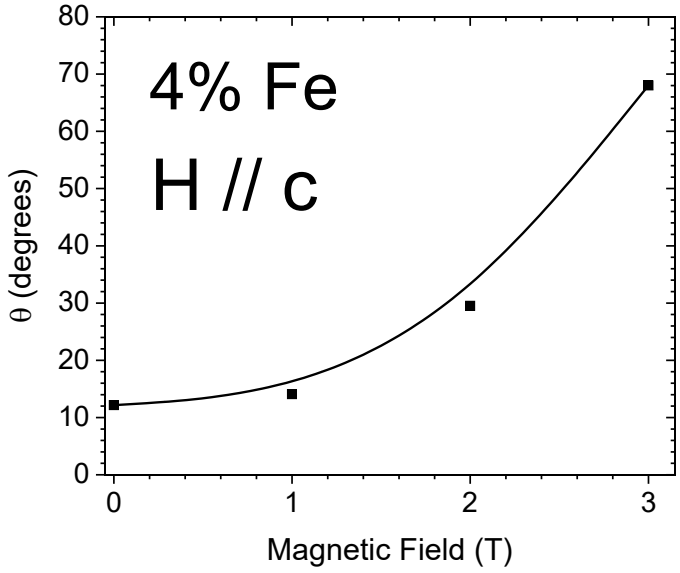

Figure 3.3.3: Angle between the cycloidal and bc planes for several magnetic fields applied along the c axis. θ is estimated through Eq.3.3.1, where the values of P_a and P_c are taken at the lowest measured temperature.

It is striking to observe such behavior of θ. In fact, even though the cycloidal makes an angle with the bc plane of only 12º at 0 T, that angle increases to nearly 70º with an applied magnetic field along the c axis of only 3 T. Thus, these results suggest that, in $TbMn_{0.96}Fe_{0.04}O_3$, an applied magnetic field along the c axis gradually rotates the cycloidal plane towards the ab plane. In principle, such gradual rotation should make P_a increase and P_c decrease with increasing field, at least in the $0 - 3$ T range. However, it is observed that, although not at the same rate, both decrease with increasing field. To gain further insight into the mechanisms here in play, the pyroelectric current along the c axis should be measured at higher fields. It would also be interesting to perform pyroelectric current measurements with an applied magnetic field along both the a and c axes in the compound with $x = 0.02$. However, due to the aforementioned technical difficulties, such measurements will also be left for future work. Neutron diffraction measurements are also clearly called for in this compound to ascertain the magnetic structure and how it is affected by a magnetic field.

3.4 Summary

Regarding $TbMn_{0.98}Fe_{0.02}O_3$, it was observed that, similarly to $TbMnO_3$, a polarization flop from the c to the a axis occurs when a magnetic field is applied along the b axis. From neutron diffraction measurements, the commensurability of the cycloidal phase seems to be irrelevant to the appearance of ferroelectricity, even though both the presence of Fe^{3+} and an applied magnetic field clearly affect it. Also, the overall decrease in polarization with increasing applied magnetic field is shown to be due to an enhancement of a spin-canting roughly along the a axis, disrupting the cycloidal spin order. In $TbMn_{0.96}Fe_{0.04}O_3$, it was seen that magnetic fields applied along either the a or b axes lead to a suppression of ferroelectricity. Also, unlike in $TbMnO_3$, a polarization flop seems to occur when a magnetic field is applied along the c axis. This might explain the striking difference between the magnetic isotherms along the c axis of this compound and $TbMnO_3$. Because of the similarity between the magnetic isotherms of $TbMnO_3$ and $TbMn_{0.98}Fe_{0.02}O_3$, one may speculate that such flop will also not be present in the latter. The results presented in this chapter suggest that the increase of 2% in the concentration of Fe^{3+} between $TbMn_{0.98}Fe_{0.02}O_3$ and $TbMn_{0.96}Fe_{0.04}O_3$ alters the physical properties in a much more extensive way than between $TbMnO_3$ and $TbMn_{0.98}Fe_{0.02}O_3$.

Chapter 4

Electromagnons in $TbMn_{0.96}Fe_{0.04}O_3$

The absence of both time and space inversion symmetries can produce a rich array of novel magnetoelectric phenomena, one of which being the coupling between the low-lying magnetic and lattice excitations to produce spin waves that are strongly coupled with optical phonons. The result of this coupling is a spin wave that can be exited by the electric component of the impinging radiation in the THz range, through an electric dipole interaction. Such spin waves are known as electromagnons. As an electromagnon can be excited by electric fields, it couples much more strongly to light than the usual magnetic dipole excitation of magnons corresponding to antiferromagnetic resonance (AFMR) [38]. This chapter is devoted to reporting a complete set of optical spectra in the $10 - 90\,cm^{-1}$ range of the multiferroic $TbMn_{0.96}Fe_{0.04}O_3$ and comparing it to previously published results in the parent compound, $TbMnO_3$, in order to unravel the behavior of the strong electric-dipole spin excitations and how they are affected by the presence of Fe^{3+}.

Both the real, n, and the imaginary, k, parts of the complex index of refraction were obtained at fixed temperatures for all the crystallographically independent orientations of the electric, E^{ω}, and magnetic, H^{ω}, components of the incoming radiation. Figure 4.0.1 shows the spectra of n in the $10 - 90\,cm^{-1}$ spectral range for $TbMn_{0.96}Fe_{0.04}O_3$. When $E^{\omega} \parallel b, c$, regardless of the direction of H^{ω}, there is no significant temperature dependence of the spectra. However, for $E^{\omega} \parallel a$, interesting features are observed. For $H^{\omega} \parallel b$, it is observed that, up to $80\,cm^{-1}$, n is temperature independent above $50\,K$ (see Fig.4.0.1 (a)). At 30 K, a decrease in n is detected in the $30 - 80\,cm^{-1}$ spectral range. Upon further cooling and in the same spectral range, n is again temperature independent. Below , a broad feature emerges when cooling from 100 K. When $H^{\omega} \parallel c$, similar behaviors are observed (see Fig.4.0.1 (b)).

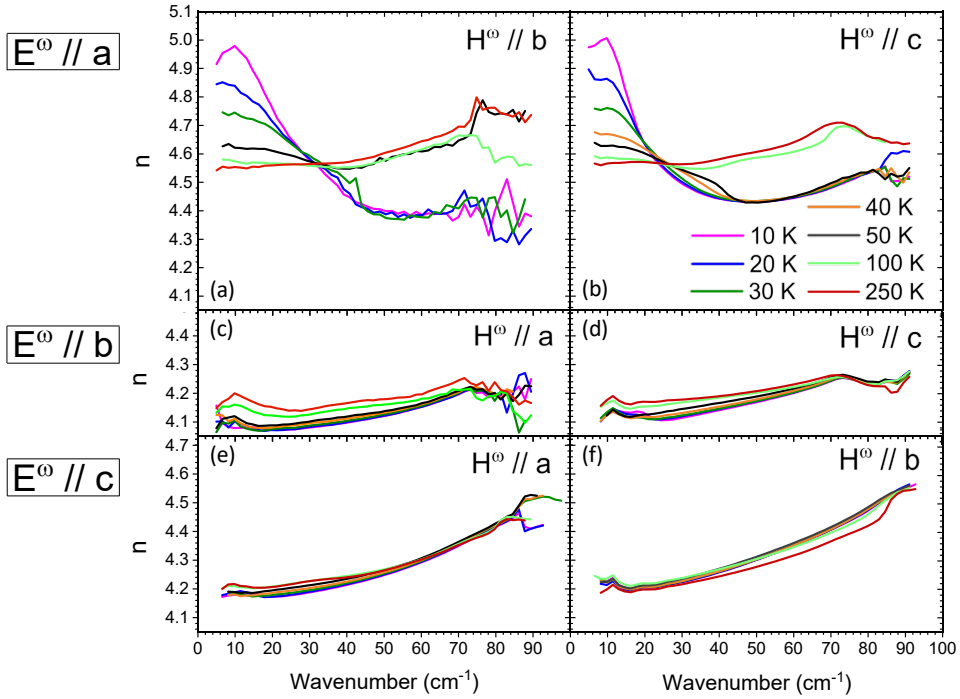

Figure 4.0.1: Spectra of the real part of the complex index of refraction, n, of $TbMn_{0.96}Fe_{0.04}O_3$ in the $10 - 90\,cm^{-1}$ spectral range, measured at fixed temperatures for all the crystallographically independent orientations of the electric, E^{ω}, and magnetic, H^{ω}, components of the incoming radiation.

The $Im[\epsilon\mu] = 2nk$ spectra of $TbMn_{0.96}Fe_{0.04}O_3$ in the $10 - 90\,cm^{-1}$ spectral range is depicted in Fig.4.0.2. For $E^{\omega} \parallel b, c$, it is observed that $Im[\epsilon\mu]$ is temperature independent above 100 K, in the whole spectral range. An eye catching feature is a sudden drop in $Im[\epsilon\mu]$ above $30\,cm^{-1}$, detected at 100 K. Upon further cooling, $Im[\epsilon\mu]$ becomes again temperature independent in the whole spectral range. The same is seen in n when $E^{\omega} \parallel a$, although for $H^{\omega} \parallel b$ it happens only below 50 K. Interestingly, this jump in the absorption happens around the same temperature as a broad peak at roughly 120 K is observed in the magnetization along the c axis (see Fig.3.1.2). While the origin of such peak remains unknown, it is now known that it might be related with changes in the absorption spectra.

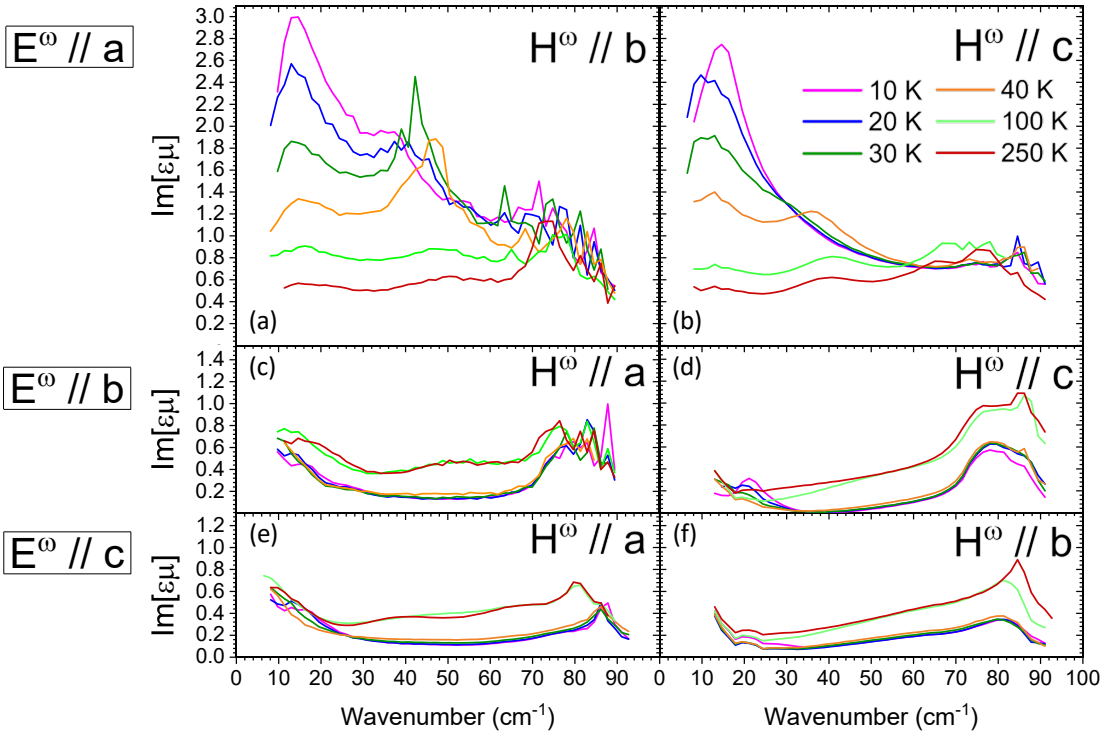

Figure 4.0.2: Temperature dependence of the $Im[\epsilon\mu]$ spectra in the $10 - 90\,\mathrm{cm}^{-1}$ range of $TbMn_{0.96}Fe_{0.04}O_3$ for all the $(E^\omega,\, H^\omega)$ polarization configurations of the incoming radiation.

Below 30 K, a tiny peak is detected around $20\,\mathrm{cm}^{-1}$ in the $(E^\omega \parallel b,\, H^\omega \parallel c)$ configuration. Since this absorption peak is only active for $H^\omega \parallel c$, i.e., it is not observed in the $(E^\omega \parallel b,\, H^\omega \parallel a)$ configuration, it is attributed to a conventional AFM resonance. A similar peak was reported and the same assignment was made in $TbMnO_3$ [42]. The development of a continuum-like absorption band composed of two broad bands peaking around 15 and 40 cm^{-1} is clearly seen with decreasing temperature. This enhancement of $Im[\epsilon\mu]$ is observed only for $E^\omega \parallel a$, irrespective of the direction of H^ω. The observed excitations are, therefore, assigned to electromagnons, which is consistent with previous observations in $TbMnO_3$ [41, 42], $DyMnO_3$ [43], $GdMnO_3$ [44] and $Eu_{1-x}Y_xMnO_3$ [46, 67]. Interestingly, such excitations are already discernible at 250 K, a much higher temperature than T_N. A similar behavior was observed in $TbMnO_3$, being ascribed to an anisotropic development of short-range spin order well above T_N [42]. Thus, it can be that the electromagnons are still active deep within the paramagnetic phase. This was reported for the multiferroic $CaMn_7O_{12}$ and the excitations were termed paraelectromagnons [68]. Again, this seems to correlate with the high temperature broad peak in magnetization around 120 K (see Fig.3.1.2) and can be due to short-range magnetic order above T_N. Nonetheless, further studies are needed to clarify this question.

With decreasing temperature, the intensity of the two bands largely increases near 40 K. Below T_N, in both the magnetically ordered phases, the relative spectral weights of the electromagnons are temperature dependent, pointing towards an energy transfer be-

tween the two excitations. Actually, the lower energy electromagnon (LE-EMG) becomes more intense, while the opposite happens to the higher energy one (HE-EMG). To make the discussion more quantitative, one can define a normalized integrated spectral weight per Mn site, S, as [42]:

$$S = C \int \omega Im[\epsilon\mu] d\omega, \tag{4.0.1}$$

where C is a constant so that $0 \leq S \leq 1$. The temperature dependence of the normalized spectral weight of both the HE-EMG and the LE-EMG is depicted in Fig. 4.0.3.

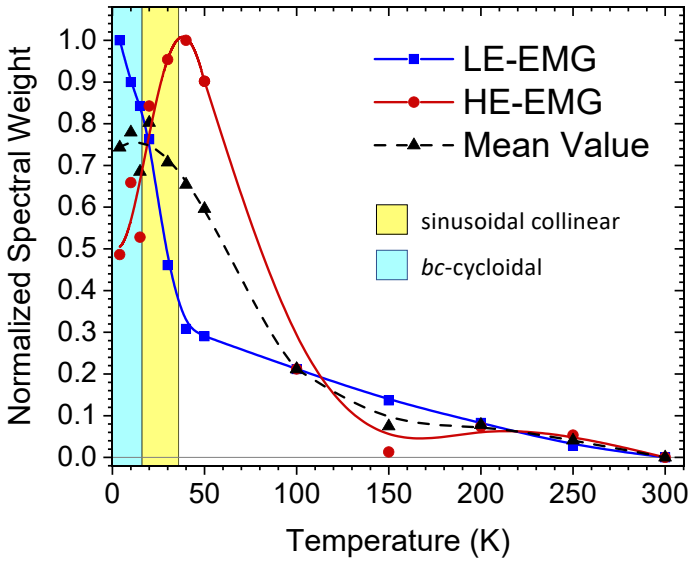

Figure 4.0.3: Temperature dependence of the normalized spectral weight for the lower (LE-EMG) and higher (HE-EMG) energy electromagnons in the $(E^{\omega} \parallel a, H^{\omega} \parallel b)$ configuration. The the mean value of the spectral weights of both electromagnons as a function of temperature is also shown. All the lines are merely a guide for the eye.

The spectral weight exhibits significant variations at temperatures considerably higher than T_N. With decreasing temperature, the HE-EMG's intensity starts to significantly increase already from roughly 100 K, a much higher temperature than T_N. As previously mentioned, this is ascribed to an anisotropic development of short-range spin order well above T_N. It is also reasonable that the development of the absorption band shows strong correlation with the formation of long-range order because its response reflects the generation of magnons with small wave number [42]. In contrast, the LE-EMG's spectral weight exhibits a rapid build-up from T_N and the rate at which it increases slightly reduces in the cycloidal phase. Interestingly, the HE-EMG's intensity rapidly decreases below T_N.

From Fig. 4.0.3, the HE-EMG has maximum spectral weight at T_N (100%), decreasing to $\sim 80\%$ at T_c and further reducing to 48% at the lowest measured temperature, T_{min}. On the other hand, the LE-EMG has a spectral weight around 32% at T_N, increasing to 76% at T_c and reaching its maximum at T_{min}. Between T_N and T_c, the HE-EMG's spectral weight reduces by $\sim 20\%$ while the LE-EMG's increases around 44%. Also, from T_c to T_{min}, the

HE-EMG's spectral weight further reduces by $\sim 32\%$, while the LE-EMG's increases by a similar amount (24%). Therefore, the two electromagnons appear to be strongly coupled in the magnetically ordered phases. Such coupling appears to be particularly strong in the cycloidal phase, as the transfer of spectral weight seems to be almost only between both electromagnons. This is nicely seen in the mean value of the spectral weights, which is roughly constant below T_c. In the sinusoidal phase, the HE-EMG's reduction in spectral weight doesn't fully account for the increase seen in the LE-EMG's, implying that there should be at least one more relevant coupling mechanism at play. Following what was observed in $GdMnO_3$, $Eu_{0.75}Y_{0.25}MnO_3$ and $TbMnO_3$, a coupling between both electromagnons and the lowest optical phonon is to be expected [42, 44, 46]. Unfortunately, due to insufficient area of the samples, it was not possible to perform temperature dependent far-infrared spectroscopy measurements, which would be able to probe higher energies and ascertain if such coupling is actually present.

There are several differences between the electromagnon's behavior in $TbMnO_3$ and in the Fe^{3+}-substituted compound. Even though the selection rule remains the same and the peak positions are roughly similar, the most striking difference is perhaps the interplay between both excitation's spectral weight. In $TbMnO_3$, no transfer of spectral weight between electromagnons was reported and the disappearance of the HE-EMG with decreasing temperature is not observed. Actually, quite the opposite happens as the HE-EMG is much more intense than the LE-EMG at low temperatures. The complex and different behavior of the electromagnons between the pure and the substituted compound demonstrates the striking differences in the magnetoelectric coupling induced by only a very small amount of Fe^{3+}.

Chapter 5

Spin-Phonon Coupling in $TbMn_{1-x}Fe_xO_3$ with x = 0, 0.02, 0.04

To take one step further towards understanding the microscopic mechanisms in the multiferroic region of the $TbMn_{1-x}Fe_xO_3$ system, spin-phonon coupling is investigated in the compounds with x = 0, 0.02 and 0.04 through Raman scattering experiments. As previously mentioned, the structure of $RMnO_3$ is described by the $Pbnm$ space group. From group theory considerations, the Raman-active phonons transform accordingly to the reducible representation $\Gamma_{Raman} = 7A_g + 5B_{1g} + 7B_{2g} + 5B_{3g}$ [69]. Representative unpolarized Raman spectra of $TbMnO_3$, $TbMn_{0.98}Fe_{0.02}O_3$ and $TbMn_{0.96}Fe_{0.04}O_3$ recorded at 10 K and 300 K in the $100 - 800\,cm^{-1}$ spectral range are shown in Fig.5.0.1. The Raman mode assignment of the bands observed in the $280 - 615\,cm^{-1}$ spectral range for $TbMnO_3$ was published by Iliev et al. [69]. By studying the Raman spectra of $TbMn_{1-x}Fe_xO_3$ for $0 \leq x \leq 1$ at room conditions, R. Vilarinho found that, since the space group and atomic position's symmetries of the atoms are maintained, the predicted Raman-active vibration modes remain the same throughout the entire series [15]. Therefore, the mode assignment of $TbMnO_3$ below $280\,cm^{-1}$ was taken to be the same as $TbFeO_3$. The Raman-active vibration modes below $200\,cm^{-1}$ are mainly characterized by displacements of the heavy rare-earth ions and, above $300\,cm^{-1}$, motions of the oxygen ions dominate. In the intermediate frequency range ($200 - 300\,cm^{-1}$), vibration patterns involve both ions. It should be stressed that both the Fe^{3+} and Mn^{3+} ions occupy centers of inversion in the $Pbnm$ structure and, therefore, vibrations involving them are not Raman active. The mode assignment of the Raman bands that will be addressed in this dissertation is shown in Table 5.0.1.

Symmetry	Wavenumber (cm^{-1})	Main atomic motion
B_{2g}	612	$Mn-O2$ stretching, in phase
A_g	378	$[110]$ MnO_6 rotation, out of phase
B_{2g}	164	$Tb(x)$, out of phase
A_g	141	$Tb(z)$, out of phase

Table 5.0.1: Symmetry, wavenumber and main atomic motions of the Raman bands assigned to the Tb^{3+} and MnO_6 motions in $TbMnO_3$ that will be addressed in this dissertation. $Tb(x)$ and $Tb(z)$ denote the Raman Tb^{3+} oscillations along the x and z axis, respectively. Data taken from [15, 69].

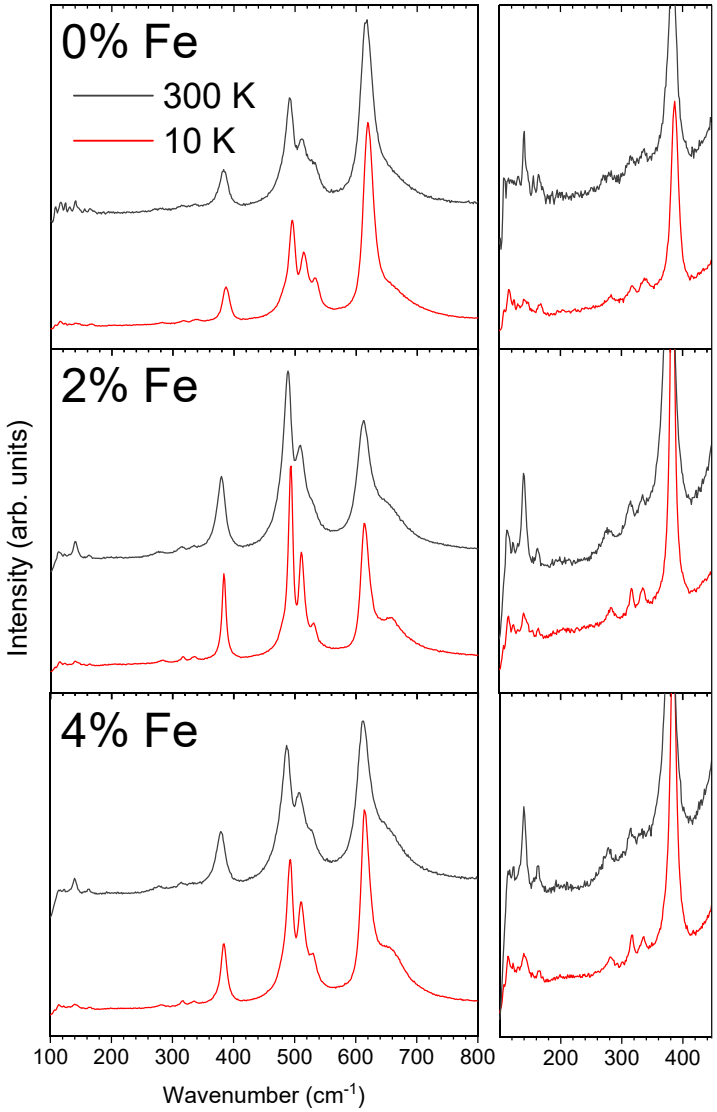

Figure 5.0.1: (left panel) Representative unpolarized Raman spectra in the $100-800\,cm^{-1}$ spectral range, recorded at $10\,K$ and $300\,K$, of $TbMn_{1-x}Fe_xO_3$, for x $= 0, 0.02$ and 0.04. (right panel) Enlarged view of the $100-420\,cm^{-1}$ spectral range.

For a given x, at first glance, no striking features are observed in the temperature evolution of the Raman spectra. With decreasing temperature, the Raman bands become better resolved and shift to higher frequencies due to volume contraction. The appearance of new Raman bands is not observed, which is particularly remarkable in the ferroelectric phase due to symmetry breaking (see section 1.4). This is because both the lattice distortions and electric polarization are small enough to conceal the clear appearance of Raman bands due to symmetry breaking in the magnetically ordered phases. However, a detailed quantitive analysis of the Raman spectra reveals interesting temperature dependences of the wavenumbers of some modes. The wavenumber at a given temperature, $\omega(T)$, of each Raman mode is obtained by the best fit of the Raman spectra with a sum of damped oscillators (Eq.2.6.1). In the temperature range where no anomalous behavior is observed, the temperature dependence of the wavenumber of the Raman modes that best sense the phase transitions taking place in these compounds, as well as their underlying mechanisms, can be well described by the normal anharmonic temperature effect due to volume contraction as temperature decreases. Taking into account up to three-phonon processes, $\omega(T)$ is given by [70]:

$$\omega(T) = \omega_0 + C\left[1 + \frac{2}{e^x - 1}\right], \tag{5.0.1}$$

with $x \equiv \hbar\omega_0/2k_BT$ and where ω_0 and C are model constants, $\hbar$ is the reduced Planck constant and k_B is the Boltzmann constant. Figure 5.0.2 shows the temperature dependence of the wavenumber of the Raman modes in Table 5.0.1 for $TbMnO_3$, $TbMn_{0.98}Fe_{0.02}O_3$ and $TbMn_{0.96}Fe_{0.04}O_3$. The solid line was obtained from the best fit of Eq.5.0.1 in the temperature range where no anomalous behavior is observed and is extrapolated to cover the $0 - 320$ K temperature range. It is evident that some modes exhibit strong deviations from the expected behavior and, in order to understand them, it becomes necessary to consider spin-phonon coupling. The frequency shift of a given phonon as a function of temperature due to the spin-phonon coupling is determined by the spin correlation function [71]:

$$\omega = \omega_0 + \gamma \left\langle \bar{S}_i \,\middle|\, \bar{S}_j \right\rangle, \tag{5.0.2}$$

where ω is the phonon frequency at a fixed temperature, ω_0 is the frequency in the absence of spin-phonon coupling and γ is the spin-phonon coupling constant. In the presence of competing FM and AFM interactions, as in $TbMnO_3$, it was proposed that the frequency shift, $\omega - \omega_0$, can be written as [71, 72]:

$$\omega - \omega_0 \propto -R_{FM} \left\langle \bar{S}_i \,\middle|\, \bar{S}_j \right\rangle + R_{AFM} \left\langle \bar{S}_i \,\middle|\, \bar{S}_k \right\rangle, \tag{5.0.3}$$

where R_{FM} and R_{AFM} are spin-dependent force constants of the lattice vibrations deduced as the squared derivatives of the exchange integrals with respect to the phonon dis-

placements. The constants R_{FM} and R_{AFM} are associated with the FM nearest-neighbor and AFM next-nearest neighbor exchanges, respectively [71, 72]. This model predicts negative or positive frequency shifts depending on the relative strength between the FM and AFM exchange interactions, associated with the eigenmode being considered. The spin correlation functions of the nearest and next-nearest neighbors are typically considered to have almost the same temperature dependence, and thus, the same correlation functions are taken for $\langle \bar{S}_i \,|\, \bar{S}_j \rangle$ and $\langle \bar{S}_i \,|\, \bar{S}_k \rangle$ [72, 73]. Moreover, when dealing with the same eigenmode, constant values for R_{FM} and R_{AFM} are assumed [72]. Thus, Eq.5.0.3 can be written as:

$$\omega - \omega_0 \propto (R_{AFM} - R_{FM}) \langle \bar{S}_i \,|\, \bar{S}_j \rangle . \tag{5.0.4}$$

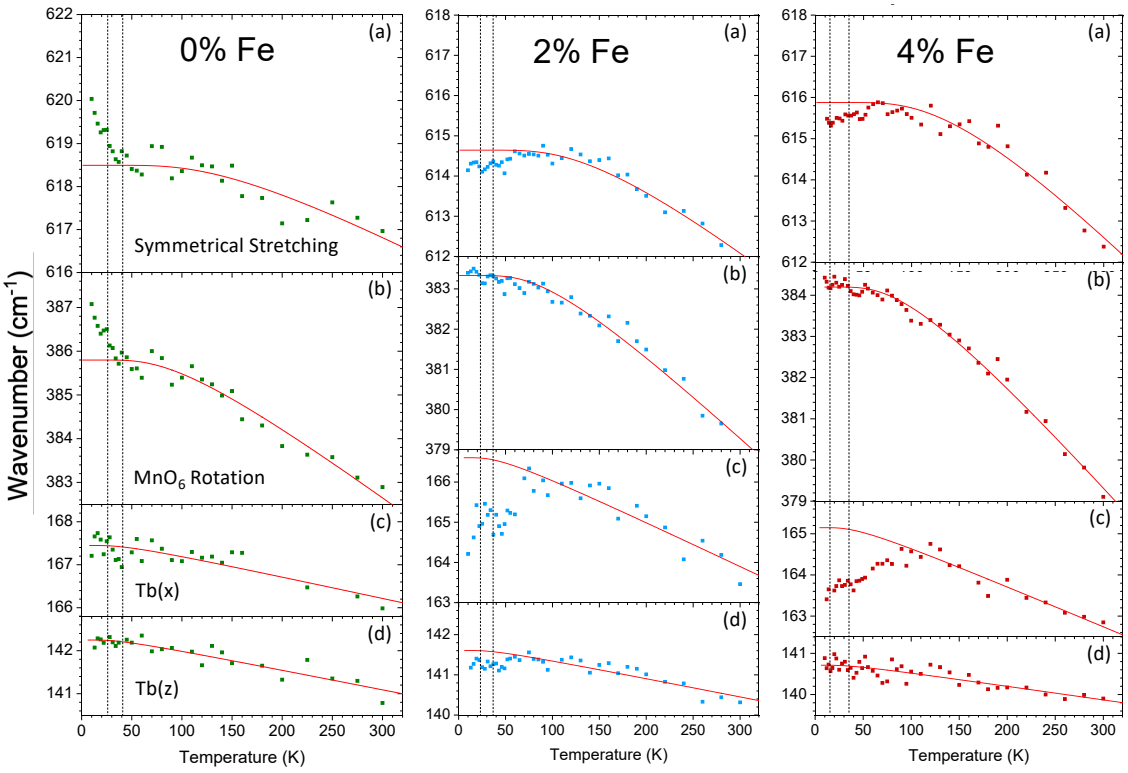

Figure 5.0.2: Temperature dependence of the wavenumber of the Raman modes for $TbMnO_3$ (left panel), $TbMn_{0.98}Fe_{0.02}O_3$ (middle panel) and $TbMn_{0.96}Fe_{0.04}O_3$ (right panel). The best fit of Eq.5.0.1 in the temperature range where no anomalous behavior is observed is represented by a solid line and is extrapolated to cover the whole temperature range ($0-320$ K). In each panel, the dashed line at the lowest temperature marks T_c while the other marks T_N.

Regarding $TbMnO_3$, apart from the modes involving rare-earth shifts, a positive frequency shift is always observed roughly below T_N, corroborating the prevalence of the AFM interactions over the FM ones in the magnetic phases below that temperature. In $TbMn_{0.98}Fe_{0.02}O_3$ and $TbMn_{0.96}Fe_{0.04}O_3$, apart from the amplitude of the deviations, the

results are quite similar. The totally symmetric stretching mode, involving the $Mn-O2$ bonds, exhibits an upwards deviation in $TbMnO_3$ and a downwards one in the substituted compounds. This mode clearly has a strong influence in the exchange integrals, being the one that best evidences the strengthening of the FM interactions over the AFM ones with increasing x. The mode related with octahedra tilting senses the magnetic interactions in $TbMnO_3$. However, it ceases to do so in the substituted compound, nicely following the behavior predicted by Eq.5.0.1. The $Tb(x)$ mode becomes sensitive to the magnetic interactions only in the substituted compounds, exhibiting a quite large downward deviation of approximately $2\,cm^{-1}$. On the other hand, further demonstrating the strong anisotropic character of these systems, the $Tb(z)$ mode practically does not sense the magnetic interactions in any of the compounds.

Regarding $TbMnO_3$, apart from the modes involving rare-earth shifts, a positive frequency shift is always observed roughly below T_N, corroborating the prevalence of the AFM interactions over the FM ones in the magnetic phases below that temperature. In $TbMn_{0.98}Fe_{0.02}O_3$ and $TbMn_{0.96}Fe_{0.04}O_3$, apart from the amplitude of the deviations, the results are quite similar. The totally symmetric stretching mode, involving the $Mn-O2$ bonds, exhibits an upwards deviation in $TbMnO_3$ and a downwards one in the substituted compounds. This mode clearly has a strong influence in the exchange integrals, being the one that best evidences the strengthening of the FM interactions over the AFM ones with increasing x. The mode related with octahedra tilting senses the magnetic interactions in $TbMnO_3$. However, it ceases to do so in the substituted compound, nicely following the behavior predicted by Eq.5.0.1. The $Tb(x)$ mode becomes sensitive to the magnetic interactions only in the substituted compounds, exhibiting a quite large downward deviation of approximately $2\,cm^{-1}$. On the other hand, further demonstrating the strong anisotropic character of these systems, the $Tb(z)$ mode practically does not sense the magnetic interactions in any of the compounds.

In $TbMnO_3$, the Tb^{3+} oscillations are not sensitive to the magnetic interactions, which appears to indicate that those ions do not significantly interact with the Mn^{3+} sublattice. This seems to corroborate the usual assumption in most theoretical models of neglecting the role of the magnetism of the Tb^{3+} ions in the dynamics and magnetic interactions behind the observed phase sequence of $TbMnO_3$. However, by adding only up to 4% of Fe^{3+}, the $Tb(x)$ mode becomes sensitive to the compound's magnetism. This indicates that the Tb^{3+} spins begin to interact with the Mn^{3+}/Fe^{3+} sublattice, as observed in $TbFeO_3$ [74]. Therefore, such interaction must involve the Fe^{3+} spins, even though their ordering should be strongly influenced by the Mn^{3+} spins, as these are in majority and dominate the magnetism. It is also interesting that, even though the modes in $TbMnO_3$ start to deviate roughly below T_N, the ones in the compounds with Fe^{3+} deviate at considerably higher temperatures. In particular, the $Tb(x)$ mode starts to deviate already below 100 K. The jump in absorption seen in THz spectroscopy, together with the broad peak in magnetization and the appearance of spin-phonon coupling, all near 100 K, seem to point towards some sort of short-range magnetic ordering below that temperature. Thus,

precursor effects in these compounds seem to play an important role and clearly deserve to be further studied. Furthermore, the difference in the behavior of the modes in the substituted compounds relatively to $TbMnO_3$ point towards an emerging FM character of the magnetic structures and are in accordance with the results from magnetization, neutron diffraction and polar measurements previously presented.

Chapter 6

Conclusions

Regarding $TbMn_{0.98}Fe_{0.02}O_3$, it was observed that, similarly to $TbMnO_3$, a polarization flop from the c to the a axis occurs when a magnetic field is applied along the b axis. From neutron diffraction measurements, the commensurability of the cycloidal phase seems to be irrelevant to the appearance of ferroelectricity, even though both the presence of Fe^{3+} and an applied magnetic field clearly affect it. Also, the overall decrease in polarization with increasing applied magnetic field is shown to be due to an enhancement of a spin-canting roughly along the a axis, disrupting the cycloidal spin order.

In $TbMn_{0.96}Fe_{0.04}O_3$, it was seen that a magnetic field applied along either the a or b axes leads to a suppression of ferroelectricity, wherein in $TbMnO_3$, a polarization flop occurs. Also, differently from $TbMnO_3$, a polarization flop seems to occur when a magnetic field is applied along the c axis. This might explain the striking difference between the magnetic isotherms along the c axis of this compound and $TbMnO_3$. The obtained results suggest that an increase of 2% in the concentration of Fe^{3+} between $TbMn_{0.98}Fe_{0.02}O_3$ and $TbMn_{0.96}Fe_{0.04}O_3$ alters the physical properties in a much more extensive way than between $TbMnO_3$ and $TbMn_{0.98}Fe_{0.02}O_3$.

It was also found that, in $TbMnO_3$, the Raman active Tb^{3+} oscillations are not sensitive to the magnetic interactions, which appears to indicate that those ions do not significantly interact with the Mn^{3+} sublattice. However, by adding only up to 4% of Fe^{3+}, the Raman mode associated with Tb^{3+} oscillations along the x axis becomes sensitive to the compound's magnetism. This indicates that the Tb^{3+} spins begin to interact with the Mn^{3+}/Fe^{3+} sublattice. Therefore, such interaction must involve the Fe^{3+} spins, even though their ordering should be strongly influenced by the Mn^{3+} spins, as these are in majority and dominate the magnetism. Remarkably, the Raman mode associated with Tb^{3+} oscillations along the z axis practically does not sense the magnetic interactions in any of the compounds, further demonstrating the strong anisotropic character of these systems.

In $TbMn_{0.96}Fe_{0.04}O_3$, differently from what has been reported in $TbMnO_3$, the two electromagnons appear to be strongly coupled in the magnetically ordered phases. Such coupling seems to be particularly strong in the cycloidal phase. However, in the sinusoidal

phase it is clear that at least one more relevant coupling mechanism is at play, most likely a coupling between both electromagnons and the lowest optical phonon. Interestingly, as in $TbMnO_3$, such excitations are already discernible at 250 K, a much higher temperature than T_N. This, together with the high temperature broad peak in magnetization around 120 K observed in all compounds and a jump in absorption detected at 100 K in $TbMn_{0.96}Fe_{0.04}O_3$, point towards a development of short-range spin order well above T_N. Thus, precursor effects in these compounds seem to play an important role and clearly deserve to be further studied.

Furthermore, the results from magnetization, neutron diffraction and polar measurements, together with the difference in the behavior of the Raman modes in the substituted compounds relatively to $TbMnO_3$, all point towards an emerging FM character of the magnetic structures of the substituted compounds. Although this dissertation brought more insight into the microscopic mechanisms underlying the substituted compounds, some questions remain unanswered. Namely, how the electromagnons couple between themselves and to the optical phonons, the origin of the high temperature magnetization broad peak and what mechanisms lie behind the apparent emergence of short-range magnetic order well above T_N.

6.1 Future Work

Although the polar and dielectric characterization in the compounds with $x = 0.02$ and 0.04 must be completed, it is clear that neutron diffraction measurements are clearly called for to ascertain the magnetic structure and how it is affected by a magnetic field, at least in the compound with $x = 0.04$. As neutron diffraction measurements in $TbMnO_3$ with magnetic field applied along the b axis are not reported and the measurements in the compound with $x = 0.02$ did not allow a refinement of the magnetic structure, they should also be performed. Also, to understand how the observed electromagnons couple to optical phonons, it would be interesting to carry out Fourier Transform Infrared Spectroscopy (FTIR) measurements. Furthermore, to gain insight on how the electromagnons are affected by an applied magnetic field, THz time-domain spectroscopy measurements with applied magnetic field should be carried out in $TbMn_{0.96}Fe_{0.04}O_3$.

It should be mentioned that all measurements left as future work were not performed during this dissertation mainly because they rely on proposals to large scale infrastructures or on equipment that is not available at IFIMUP. However, proposals to such infrastructures are underway and a fruitful collaboration with FZU will allow to complete most of these measurements in the near future.

References

[1] Hans Schmid, Multiferroic magnetoelectrics, *Ferroelectrics*, **162**, 317–338, (1994).

[2] Daniel Khomskii, Classifying multiferroics: Mechanisms and effects, *Physics*, **2**, (2009).

[3] L. D. Landau and E. M Lifshitz. *Electrodynamics of continuous media*. Moscow: Fizmatgiz, (1959).

[4] D. Schlom, B. Liu, R. Ramesh, M. Wuttig, N. Spaldin, U. Waghmare, J. Wang, J. Neaton, V. Vaithyanathan, D. Viehland, S. Ogale, K. Rabe, V. Nagarajan and H. Zheng, Epitaxial BiFeO3 Multiferroic Thin Film Heterostructures, *Science*, **299**, 1719–1722, (2003).

[5] T. Kimura, G. Lawes, T. Goto, Y. Tokura and A. P. Ramirez, Magnetoelectric phase diagrams of orthorhombic RMnO3 (R=Gd, Tb, and Dy), *Physical Review B - Condensed Matter and Materials Physics*, **71**, 1–13, (2005).

[6] Shuai Dong, Jun Ming Liu, Sang Wook Cheong and Zhifeng Ren, Multiferroic materials and magnetoelectric physics: Symmetry, entanglement, excitation, and topology, *Advances in Physics*, **64**, 519–626, (2015).

[7] N. A. Spaldin and R. Ramesh, Advances in magnetoelectric multiferroics, *Nature Materials*, **18**, 203–212, (2019).

[8] Nicola A. Hill, Why Are There so Few Magnetic Ferroelectrics?, *The Journal of Physical Chemistry B*, **104**, 6694–6709, (2002).

[9] J Wang, J Wang, J B Neaton, H Zheng, V Nagarajan and S B Ogale, Epitaxial BiFeO3 Multiferroic Thin Film Heterostructures, *Science*, **299**, 1719–1722, (2003).

[10] T. Kimura, T. Goto, H. Shintani, K. Ishizaka, T. Arima and Y. Tokura, Magnetic control of ferroelectric polarization, *Nature*, **426**, 55–58, (2003).

[11] A. M. Glazer, The classification of tilted octahedra in perovskites, *Acta Crystallographica Section B Structural Crystallography and Crystal Chemistry*, **28**, 3384–3392, (1972).

[12] Victor M. Goldschmidt, Die Gesetze der Krystallochemie, *Die Naturwissenschaften*, **21**, 477, (1926).

[13] Patrick M. Woodward, Octahedral Tilting in Perovskites. I. Geometrical Considerations, *Acta Crystallographica Section B: Structural Science*, **53**, 32–43, (1997).

[14] D. J. Passos. *From manganites to ferrites: a study on the structural, magnetic and magnetoelectric properties, MSc Thesis.* PhD thesis, University of Porto, (2015).

[15] R. Vilarinho. *From Structural Distortions to Physical Properties in Orthorhombic Rare-Earth Perovskites*. Phd thesis, University of Porto, (2019).

[16] Peng Chen, Mathieu N. Grisolia, Hong Jian Zhao, Otto E. González-Vázquez, L. Bellaiche, Manuel Bibes, Bang Gui Liu and Jorge Íñiguez, Energetics of oxygen-octahedra rotations in perovskite oxides from first principles, *Physical Review B*, **97**, 1–22, (2018).

[17] H. A. Jahn and E. Teller, Stability of polyatomic molecules in degenerate electronic states, *Proceedings of the Royal Society of London. Series A - Mathematical and Physical Sciences*, **161**, 220–235, (1937).

[18] J. M. Perez-Mato, D. Orobengoa and M. I. Aroyo. *Mode crystallography of distorted structures*, volume 66. International Union of Crystallography, (2010).

[19] Michael A. Carpenter and Christopher J. Howard, Symmetry rules and strain/order-parameter relationships for coupling between octahedral tilting and cooperative Jahn-Teller transitions in ABX 3 perovskites. II. Application, *Acta Crystallographica Section B: Structural Science*, **65**, 147–159, (2009).

[20] M. Mihalik, M. Mihalik, Z. Jagličić, R. Vilarinho, J. Agostinho Moreira, E. Queiros, P. B. Tavares, A. Almeida and M. Zentková, Magnetic phase diagram of the TbMn1−xFexO3solid solution system, *Physica B: Condensed Matter*, **506**, 163–167, (2017).

[21] R. Vilarinho, E. Queirós, D. J. Passos, D. A. Mota, P. B. Tavares, M. Mihalik, M. Zentkova, M. Mihalik, A. Almeida and J. Agostinho Moreira, On the ferroelectric and magnetoelectric mechanisms in low Fe3+doped TbMnO3, *Journal of Magnetism and Magnetic Materials*, **439**, 167–172, (2017).

[22] M. Mihalik, M. Mihalik, M. Fitta, M. Vavra, M. Zentková, R. Vilarinho, D. A. Mota, P. Tavares, J. Agostinho Moreira and A. Almeida, Heat capacity, magnetic and lattice dynamic properties of TbMn1-xFexO3, *Journal of Physics: Conference Series*, **592**, 0–6, (2014).

[23] R. Vilarinho, D. J. Passos, E. C. Queirós, P. B. Tavares, A. Almeida, M. C. Weber, M. Guennou, J. Kreisel and J. Agostinho Moreira, Suppression of the cooperative

Jahn-Teller distortion and its effect on the Raman octahedra-rotation modes of TbM n1-x F ex O3, *Physical Review B*, **97**, (2018).

[24] Masahito Mochizuki and Nobuo Furukawa, Microscopic model and phase diagrams of the multiferroic perovskite manganites, *Physical Review B - Condensed Matter and Materials Physics*, **80**, 1–22, (2009).

[25] T. Kimura, S. Ishihara, H. Shintani, T. Arima, T. Takahashi, K. Ishizaka and Y. Tokura, Distorted perovskite with eg1 configuration as a frustrated spin system, *Physical Review B - Condensed Matter and Materials Physics*, **68**, 3–6, (2003).

[26] T. Goto, T. Kimura, G. Lawes, A. P. Ramirez and Y. Tokura, Ferroelectricity and giant magnetocapacitance in perovskite rare-earth manganites, *Physical Review Letters*, **92**, 1–4, (2004).

[27] T. Arima, T. Goto, Y. Yamasaki, S. Miyasaka, K. Ishii, M. Tsubota, T. Inami, Y. Murakami and Y. Tokura, Magnetic-field-induced transition in the lattice modulation of colossal magnetoelectric GdMnO3 and TbMnO3 compounds, *Physical Review B*, **72**, 100102, (2005).

[28] M. Tokunaga, Y. Yamasaki, Y. Onose, M. Mochizuki, N. Furukawa and Y. Tokura, Novel Multiferroic State of Eu1-xYxMnO3 in High Magnetic Fields, *Physical Review Letters*, **103**, 187202, (2009).

[29] R. Kajimoto, H. Yoshizawa, H. Shintani, T. Kimura and Y. Tokura, Magnetic structure of TbMnO3 by neutron diffraction, *Physical Review B - Condensed Matter and Materials Physics*, **70**, 1–4, (2004).

[30] A. B. Harris, J. W. Lynn, M. Kenzelmann, C. Broholm, O. P. Vajk, C. L. Zhang, S.-W. Cheong, S. B. Kim, J. Schefer and S. Jonas, Magnetic Inversion Symmetry Breaking and Ferroelectricity in TbMnO3, *Physical Review Letters*, **95**, 27–30, (2005).

[31] S. Mansouri, S. Jandl, M. Balli, P. Fournier, A. A. Mukhin, V. Yu Ivanov, A. Balbashov and M. Orlita, Study of crystal-field excitations and infrared active phonons in TbMnO3, *Journal of Physics Condensed Matter*, **30**, (2018).

[32] I. A. Sergienko and E. Dagotto, Role of the Dzyaloshinskii-Moriya interaction in multiferroic perovskites, *Physical Review B - Condensed Matter and Materials Physics*, **73**, 1–5, (2006).

[33] Toru Moriya, Critical Fields of Superconducting Sn, In, and Ta, *Physical Review Letters*, **120**, 91–98, (1960).

[34] Hosho Katsura, Naoto Nagaosa and Alexander V. Balatsky, Spin current and magnetoelectric effect in noncollinear magnets, *Physical Review Letters*, **95**, 1–4, (2005).

[35] H. J. Xiang, Su Huai Wei, M. H. Whangbo and Juarez L F Da Silva, Spin-orbit coupling and ion displacements in multiferroic TbMnO3, *Physical Review Letters*, **101**, 1–4, (2008).

[36] Andrei Malashevich and David Vanderbilt, Dependence of electronic polarization on octahedral rotations in TbMnO 3 from first principles, *Physical Review B - Condensed Matter and Materials Physics*, **80**, 1–7, (2009).

[37] J. Herrero-Martin, D. F. McMorrow, A. T. Boothroyd, D. Prabhakaran, H. C. Walker, F. de Bergevin, F. Fabrizi and L. Paolasini, Femtoscale Magnetically Induced Lattice Distortions in Multiferroic TbMnO3, *Science*, **333**, 1273–1276, (2011).

[38] Markku P V Stenberg and Rogério De Sousa, Model for twin electromagnons and magnetically induced oscillatory polarization in multiferroic R MnO3, *Physical Review B - Condensed Matter and Materials Physics*, **80**, 1–5, (2009).

[39] V. G. Baryakhtar and I. E. Chupis, Phenomenological theory of a ferroelectric magnet, *Sov. Phys. Solid State*, **10**, 2818, (1969).

[40] V. G. Baryakhtar and I. E. Chupis, Quantum theory of oscillations in a ferroelectric ferromagnet, *Sov. Phys. Solid State*, **11**, 2628, (1970).

[41] A. Pimenov, A. A. Mukhin, V. Yu Ivanov, V. D. Travkin, A. M. Balbashov and A. Loidl, Possible evidence for electromagnons in multiferroic manganites, *Nature Physics*, **2**, 97–100, (2006).

[42] Y. Takahashi, N. Kida, Y. Yamasaki, J. Fujioka, T. Arima, R. Shimano, S. Miyahara, M. Mochizuki, N. Furukawa and Y. Tokura, Evidence for an electric-dipole active continuum band of spin excitations in multiferroic TbMnO3, *Physical Review Letters*, **101**, 1–4, (2008).

[43] N. Kida, Y. Ikebe, Y. Takahashi, J. P. He, Y. Kaneko, Y. Yamasaki, R. Shimano, T. Arima, N. Nagaosa and Y. Tokura, Electrically driven spin excitation in the ferroelectric magnet DyMnO3, *Physical Review B - Condensed Matter and Materials Physics*, **78**, 1–9, (2008).

[44] A. Pimenov, T. Rudolf, F. Mayr, A. Loidl, A. A. Mukhin and A. M. Balbashov, Coupling of phonons and electromagnons in GdMnO3, *Physical Review B - Condensed Matter and Materials Physics*, **74**, 9–12, (2006).

[45] Hosho Katsura, Alexander V. Balatsky and Naoto Nagaosa, Dynamical magnetoelectric coupling in helical magnets, *Physical Review Letters*, **98**, 1–4, (2007).

[46] R. Valdés Aguilar, A. B. Sushkov, C. L. Zhang, Y. J. Choi, S.-W. Cheong and H. D. Drew, Colossal magnon-phonon coupling in multiferroic Eu0.75Y0.25MnO3, *Physical Review B*, **76**, 060404, (2007).

[47] A. M. Shuvaev, V. D. Travkin, V. Yu Ivanov, A. A. Mukhin and A. Pimenov, Evidence for electroactive excitation of the spin cycloid in TbMnO3, *Physical Review Letters*, **104**, 3–6, (2010).

[48] Noriaki Kida, Yuichi Yamasaki, Ryo Shimano, Taka Hisa Arima and Yoshinori Tokura, Electric-dipole active two-magnon excitation in ab spiral spin phase of a ferroelectric magnet Gd0.7Tb0.3MnO3, *Journal of the Physical Society of Japan*, **77**, 1–4, (2008).

[49] Y Takahashi, Y Yamasaki, N Kida, Y Kaneko, T Arima, R Shimano and Y Tokura, Far-infrared optical study of electromagnons and their coupling to optical phonons in Eu1−xYxMnO3 (x=0.1, 0.2, 0.3, 0.4, and 0.45), *Physical Review B*, **79**, 214431, (2009).

[50] R. Valdés Aguilar, M. Mostovoy, A. B. Sushkov, C. L. Zhang, Y. J. Choi, S. W. Cheong and H. D. Drew, Origin of electromagnon excitations in multiferroic RMnO3, *Physical Review Letters*, **102**, 1–4, (2009).

[51] J. S. Lee, N. Kida, S. Miyahara, Y. Takahashi, Y. Yamasaki, R. Shimano, N. Furukawa and Y. Tokura, Systematics of electromagnons in the spiral spin-ordered states of R MnO3, *Physical Review B - Condensed Matter and Materials Physics*, **79**, 7–10, (2009).

[52] A. Pimenov, A. Shuvaev, A. Loidl, F. Schrettle, A. A. Mukhin, V. D. Travkin, V. Yu. Ivanov and A. M. Balbashov, Magnetic and Magnetoelectric Excitations in TbMnO3, *Physical Review Letters*, **102**, 107203, (2009).

[53] Masahito Mochizuki, Nobuo Furukawa and Naoto Nagaosa, Theory of electromagnons in the multiferroic Mn perovskites: The vital role of higher harmonic components of the spiral spin order, *Physical Review Letters*, **104**, 1–4, (2010).

[54] Markku P.V. Stenberg and Rogério De Sousa, Sinusoidal electromagnon in RMnO 3: Indication of anomalous magnetoelectric coupling, *Physical Review B - Condensed Matter and Materials Physics*, **85**, 1–5, (2012).

[55] T. Goto, Y. Yamasaki, H. Watanabe, T. Kimura and Y. Tokura, Anticorrelation between ferromagnetism and ferroelectricity in perovskite manganites, *Physical Review B - Condensed Matter and Materials Physics*, **72**, 1–4, (2005).

[56] Fang Hong, Zhenxiang Cheng, Hongyang Zhao, Hideo Kimura and Xiaolin Wang, Continuously tunable magnetic phase transitions in the DyMn 1-xFexO3 system, *Applied Physics Letters*, **99**, 3–6, (2011).

[57] Fang Hong, Binbin Yue, Jianli Wang, Andrew Studer, Chunsheng Fang, Xiaolin Wang, Shixue Dou and Zhenxiang Cheng, Collapse and reappearance of magnetic orderings in spin frustrated TbMnO3 induced by Fe substitution, *Applied Physics Letters*, **109**, (2016).

[58] Chandan De, Rabindranath Bag, Surjeet Singh, Fabio Orlandi, Pascal Manuel, Sean Langridge, Milan K. Sanyal, C. N.R. Rao, Maxim Mostovoy and A. Sundaresan, Highly tunable magnetic spirals and electric polarization in Gd 0.5 Dy 0.5 MnO 3, *Physical Review Materials*, **3**, 1–10, (2019).

[59] R. D. Shannon, Revised effective ionic radii and systematic studies of interatomic distances in halides and chalcogenides, *Acta Crystallographica Section A*, **32**, 751–767, (1976).

[60] Harikrishnan S. Nair, Tapan Chatterji, C. M.N. Kumar, Thomas Hansen, Hariharan Nhalil, Suja Elizabeth and André M. Strydom, Magnetic structures and magnetic phase transitions in the Mn-doped orthoferrite TbFeO3 studied by neutron powder diffraction, *Journal of Applied Physics*, **119**, 1–8, (2016).

[61] Yifei Fang, Ya Yang, Xinzhi Liu, Jian Kang, Lijie Hao, Xiping Chen, Lei Xie, Guangai Sun, Venkatesh Chandragiri, Chin-Wei Wang, Yiming Cao, Fei Chen, Yuntao Liu, Dongfeng Chen, Shixun Cao, Chengtian Lin, Wei Ren and Jincang Zhang, Observation of re-entrant spin reorientation in TbFe1−xMn x O3, *Scientific Reports*, **6**, 33448, (2016).

[62] W. S. Ferreira. *Estudo do Efeito Magneto-Eléctrico e suas Aplicações*. PhD thesis, University of Porto, (2011).

[63] Volodymyr Skoromets. *Tunable materials and structures for terahertz spectral range*. PhD thesis, Charles University, (2013).

[64] Petr Kužel and Jan Petzelt, Time-resolved terahertz transmission spectroscopy of dielectrics, *Ferroelectrics*, **239**, 79–86, (2000).

[65] Lionel Duvillaret, Frédéric Garet and Jean Louis Coutaz, A reliable method for extraction of material parameters in terahertz time-domain spectroscopy, *IEEE Journal on Selected Topics in Quantum Electronics*, **2**, 739–745, (1996).

[66] William Hayes and Rodney London. *Scattering of Light by Crystals*. Wiley-Interscience, volume 47 edition, (1979).

[67] A. Pimenov, A. Loidl, A. A. Mukhin, V. D. Travkin, V. Yu. Ivanov and A. M. Balbashov, Terahertz spectroscopy of electromagnons in Eu1−xYxMnO3, *Physical Review B*, **77**, 014438, (2008).

[68] Filip Kadlec, Veronica Goian, Christelle Kadlec, Martin Kempa, Přemysl Vaněk, Jon Taylor, Stéphane Rols, Jan Prokleška, Milan Orlita and Stanislav Kamba, Possible coupling between magnons and phonons in multiferroic CaMn7 O12, *Physical Review B - Condensed Matter and Materials Physics*, **90**, 1–8, (2014).

[69] M. N. Iliev, M. V. Abrashev, J. Laverdière, S. Jandl, M. M. Gospodinov, Y. Q. Wang and Y. Y. Sun, Distortion-dependent Raman spectra and mode mixing in R MnO3 perovskites (R=La,Pr,Nd,Sm,Eu,Gd,Tb,Dy,Ho,Y), *Physical Review B - Condensed Matter and Materials Physics*, **73**, 3–8, (2006).

[70] M. Balkanski, R. F. Wallis and E. Haro, Anharmonic effects in light scattering due to optical phonons in silicon, *Physical Review B*, **28**, 1928–1934, (1983).

[71] W Baltensperger and J. S. Helman, Influence of magnetic order in insulators on the optical phonon frequency, *Helvetica Physica Acta*, **41**, 668, (1968).

[72] Kunio Wakamura and Toshihiro Arai, Effect of magnetic ordering on phonon parameters for infrared active modes in ferromagnetic spinel CdCr2S4, *Journal of Applied Physics*, **63**, 5824–5829, (1988).

[73] Herbert B. Callen and Earl Callen, Cluster approximation for ferromagnets with first- and second-neighbor exchange, with application to the europium chalcogenides, *Physical Review*, **136**, (1964).

[74] Mads Christof Weber, Mael Guennou, Hong Jian Zhao, Jorge Íñiguez, Rui Vilarinho, Abílio Almeida, Joaquim Agostinho Moreira and Jens Kreisel, Raman spectroscopy of rare-earth orthoferrites RFeO3 (R =La, Sm, Eu, Gd, Tb, Dy), *Physical Review B*, **94**, 1–8, (2016).